

AD

**STRESS CONCENTRATORS AND RATE EFFECTS IN
FORMATION OF ADIABATIC SHEAR BANDS**

(Revised version)

Final Technical Report
(End of the first year 1995/96)

by Janusz R. Klepaczko

August 1996

**UNITED STATES ARMY
EUROPEAN RESEARCH OFFICE OF THE US ARMY
LONDON, ENGLAND**

CONTRACT N°: N68171-95-C-9071

Contractor:

Laboratoire de Physique et Mécanique des Matériaux
U.R.A. C.N.R.S N° 1215
Institut Supérieur de Génie Mécanique et Productique
UNIVERSITE DE METZ
F-57045 Metz, France

Approved for Public Release
Distribution unlimited

19970911 081

AD

**STRESS CONCENTRATORS AND RATE EFFECTS IN
FORMATION OF ADIABATIC SHEAR BANDS**

(Revised version)

Final Technical Report
(End of the first year 1995/96)

by Janusz R. Klepaczko

August 1996

**UNITED STATES ARMY
EUROPEAN RESEARCH OFFICE OF THE US ARMY
LONDON, ENGLAND**

CONTRACT N°: N68171-95-C-9071

DTIC QUALITY INSPECTED 4

Contractor:

Laboratoire de Physique et Mécanique des Matériaux
U.R.A. C.N.R.S N° 1215
Institut Supérieur de Génie Mécanique et Productique
UNIVERSITE DE METZ
F-57045 Metz, France

Approved for Public Release
Distribution unlimited

REPORT DOCUMENTATION PAGE			Form Approved OMB NO. 0704-0188
<small>Further information required for the collection of information is contained in section 17 of the DOD Form 1040, including the time for responding, instructions, definition of existing data source, defining and maintaining the data source, and compressing and compressing the collection of information. Some comments may apply to other forms or to other aspects of the collection of information, including suggestions for reducing this burden to the minimum. Send comments to Department of Defense, Director for Information Operations and Reports, 1215 Jefferson Davis Highway, Suite 1704, Arlington, VA 22202-4102, and to the Office of Management and Budget, Paperwork Reduction Project 0704-0188, Washington, DC 20503.</small>			
1. AGENCY USE ONLY (Leave blank)	2. REPORT DATE 31/08/96	3. REPORT TYPE AND DATES COVERED FINAL, 09/01/95-08/01/96	
4. TITLE AND SUBTITLE STRESS CONCENTRATORS AND RATE EFFECTS INFORMATION OF ADIABATIC SHEAR BANDS		5. FUNDING NUMBERS CONTRACT N N68171-95-C-9071 PROJECT N WK2Q6C-7058-AN01	
6. AUTHOR(S) J. R. KLEPACZKO			
7. PERFORMING ORGANIZATION NAME(S) AND ADDRESS(ES) METZ UNIVERSITY - I.S.G.M.P. LAB. OF PHYSICS & MECHANICS OF MATERIALS ILE DU SAULCY FR-57045 METZ, FRANCE		8. PERFORMING ORGANIZATION REPORT NUMBER N/A	
9. SPONSORING/MONITORING AGENCY NAME(S) AND ADDRESS(ES) USARDSG-UK, ENVIRONMENTAL SCIENCE BRANCH Dr. R. REICHENBACH, EDISON HOUSE 223 OLD MARYLEBONE R.D., LONDON NW1-5TH UK		10. SPONSORING/MONITORING AGENCY REPORT NUMBER	
11. SUPPLEMENTARY NOTES NONE			
12. DISTRIBUTION/AVAILABILITY STATEMENT DISTRIBUTION UNLIMITED		13. DISTRIBUTION CODE N/A	
14. ABSTRACT (Maximum 200 words) The phenomenon of shear instability and flow localization is investigated in this Report. The ultrahigh strength steel VAR 4340, ~ 52 HRC was tested in shear at wide range of the imposed velocities, from quasi-static to 120 m/s. A new experimental technique of direct impact on double shear specimen was used. Four specimen geometries were tested with different stress concentrators, from standard to a very sharp notch. At loading velocities higher than the threshold value a substantial drop of the failure strains and failure energies was observed. To study this effect a series of FE simulations was run for two notch geometries. An extended FE simulation program was performed on occurrence of the Critical Impact Velocity (CIV) in shear. The FE calculations confirmed experimental result, CIV for VAR 4340 steel ~ 52 HRC is ~ 130 m/s. A substantial drop of the localization energy was found at impact velocities higher than the CIV (130 m/s).			
15. SUBJECT TERMS ADIABATIC SHEAR BANDS, STRESS CONCENTRATORS IN IMPACT FRACTURE DYNAMIC PLASTICITY			16. NUMBER OF PAGES
			17. SECURITY CLASSIFICATION OF REPORT UNCLASSIFIED
18. SECURITY CLASSIFICATION OF THIS PAGE UNCLASSIFIED			19. SECURITY CLASSIFICATION OF ABSTRACT UNCLASSIFIED
			20. LIMITATION OF ABSTRACT

Extended abstract

An investigation was conducted into the effect of the imposed velocities, including impact up to 120 m/s, on adiabatic shear band (ASB) formation and failure for VAR 4340 steel, 52 HRC. Experiments on impact shearing have been performed on four specimen geometries with different stress concentrators, from standard geometry to a sharp notch. Each geometry was tested within a wide range of imposed velocities, from 2×10^{-6} m/s to 120 m/s, increased by 19 steps. To cover the whole rate spectrum a fast hydraulic testing machine was applied up to $V_i = 2,5$ m/s, at higher velocities a relatively new experimental technique was used. This technique is based on direct impact of a projectile on the double shear specimen, [1, 4].

For all four geometries a series of curves has been produced in the form of shear stress τ versus the nominal strain Γ_n . The characteristic points of those curves, like the instability strain Γ_{nc} and the final localization strain Γ_{nl} at failure have been found. A threshold has been identified for all four geometries between isothermal and adiabatic reaction to the imposed velocity. At velocities higher than $V_i = 0,02$ m/s ($\Gamma_n = 10$ s $^{-1}$) a substantial drop of the instability strain had occurred. This leads at higher velocities to even more pronounced drop of the failure energy for all four geometries studied. The stress concentrators act as the starters to failure.

Preliminary FE simulations performed for two different notch geometries with a complete thermal coupling, that is that the plastic work produces an increase of the local temperature and the thermal diffusion produces thermal sinks, have confirmed the experimental observations. Around the notch tips a zone of large plastic deformations and high temperatures are formed very rapidly.

Finally, an extensive FE study has been completed for VAR 4340 steel, 52 HRC, on plastic instability by wave trapping, [11, 12]. It has been found that the Critical Impact Velocity (CIV) in shear can be precisely estimated from a FE technique. Transition from quasi-static instability with thermal coupling to the CIV in shear is the PROCESS with almost instantaneous drop of the failure energy when the CIV is exceeded. A good correlation was found between the CIV values found by the FE code and experiment.

- List of Keywords:
- Adiabatic shear bands
 - High strength steels
 - VAR 4340 steel
 - Shear test
 - Dynamic plasticity
 - Shear fracture

CONTENTS

Extended abstract	2
Introduction and Objectives	4
Experimental Technique of Direct Impact on Modified Double Shear Specimen	6
Experiments on MDS Specimens with Different Stress Concentrators, VAR 4340 Steel	7
Preliminary FE Analysis of the "U" and "V" Geometries	10
FE Analysis of the Critical Impact Velocity in Shear, Technical Details	11
Results of the FE Simulations	15
Summary, Discussion and Final Conclusions	17
References	20
Tables	23
Figure captions	24

Appendixes:

Appendix N°1; M. Klosak and J.R. Klepaczko, Numerical Study of the Critical Impact Velocity in Shear

All Appendixes are under separate cover

Introduction and objectives

The main purpose of the first year of this research program was to gain more information on the effect of stress concentrators and rate effects in formation of adiabatic shear bands (ASB) and fracture. In pursuit of these goals, experimental studies on the effect of stress concentrators and impact velocities have been undertaken. The material tested was VAR 4340 steel, ~ 52 HRC. On the other hand numerical calculations with more realistic boundary conditions have been performed.

The main purpose was to investigate the discrepancy between numerical calculations and experimental results reported in [1] for 1018 annealed steel (0.18% C) and VAR 4340 steel. A finite difference computer program has been put into operation in LPMM-Metz around 1988, [2]. Recent version of this program has been modified in comparison to that used in [2] into two directions [3]. The geometry of the deformed layer was assumed the same as for the experiment, [4], and the number of elementary sublayers was increased to 100. The results of those calculations for 1018 steel are shown in Fig. 1 and Fig. 2. It is clear from those figures that both, the nominal shear strain defined as $\Gamma_n = \Delta x / h_s$, where Δx is the shear displacement and h_s is the height of the layer, and temperatures outside and inside of the ASB, increase when the nominal strain rate $\dot{\Gamma}_n = V / h_s$ increases.

This result is logical for the steady state development of the ASB when the initial conditions of the imposed velocity are not precisely defined. In other words, the imposed velocity V_i on the top of the layer already has its prescribed value without clear specification how this value has been reached. As it was concluded in [1] and [2], at high nominal strain rates the local inertia and rate sensitivity substantially delay the final stages of localization.

A series of experiments performed for 1018 steel (XC18 French Standards) with the direct impact on the Modified Double Shear (MDS) specimen [4], at impact velocities $30 \text{ m/s} \leq V \leq 100 \text{ m/s}$ (nominal strain rates $1.5 * 10^4 \text{ s}^{-1} \leq \dot{\Gamma} \leq 5 * 10^4 \text{ s}^{-1}$) has revealed a substantial differences between experimental results and numerical steady state calculations. Those experimental results are reproduced in Fig. 3. Within the region of lower nominal strain rates the trend is similar as it was predicted by the numerics, that is the nominal strain at the end of localization increases when the strain rate is increased, but at higher strain rates, or impact velocities, a substantial drop of the localization strain (fracture strain) occurs. For example, estimated mean value of the fracture strain Γ_{nf} from five tests performed at $\dot{\Gamma} = 1.5 * 10^4 \text{ s}^{-1}$ is $\Gamma_{nf} \approx 2.95$ and the mean value of three tests at $\dot{\Gamma} \approx 5 * 10^4 \text{ s}^{-1}$ is $\Gamma_{nf} \approx 1.31$. Thus, this result is in complete contradiction to the numerical

results of Fig. 1 where the stabilization effects at increasing strain rates are quite clear. In conclusion, it is easier to develop ASBs and fracture in real parts (specimen) at increased impact velocities. This effect has been confirmed for 1018 steel by evaluation of the total energy to fracture of MDS specimens, the result is shown in Fig. 4 after [1]. The drop of energy as a function of $\dot{\Gamma}$ is less intense as compared to $\Gamma_{nf}(\log \dot{\Gamma})$, mostly due to very high positive rate sensitivity of 1018 steel. Nevertheless, the mean value of the energy to fracture is reduced about twice for two impact velocities, 30 m/s and 100 m/s. Similar results were also reported in [1] for a limited series of tests on VAR 4340 steel.

A fundamental question arises why in the case of steady shearing an increase of calculated critical strains clearly occurs at strain rates higher than 10^3 s^{-1} and in the case of direct loading at different velocities with the MDS technique, [4], both critical strains and fracture energy strongly diminishes with the nominal strain rate. It is of practical interest to study further this fundamental discrepancy, experimentally and by numerical analyses.

In order to clarify the problems rised, the effect of the MDS geometry, more specifically the existing stress concentrators, was one of the objectives of this study. The Finite Elements (FE) calculations for the MDS specimen reported in [1] have shown existence of the stress concentrators around the corners present in the standard geometry. The numerical calculations for the 1018 steel were performed for the uniform layer with a small geometry imperfection, [2, 3].

To study further the effect of stress concentrators at different loading rates on formation of the ASBs four different specimen geometries were tested with increasing stress gradients.

The second specific objective involving a more realistic initial conditions imposed during experiments on the MDS specimen, was to clarify the effects of plastic waves, more specifically existence of the Critical Impact Velocity (CIV) in shear [5, 6, 7]. The FE technique has been applied for this purpose.

Experimental technique of direct impact on Modified Double Shear specimen

This relatively new experimental technique, which has been described with details in [4], is now operational in LPMM-Metz. Such technique has been already applied for 1018 steel, also a limited series of tests was performed on VAR 4340 steel (~52 HRC), [1]. Because the theory and details of this experimental technique is given elsewhere [4], here only a brief description is offered. Fig. 5 shows the principles.

The MDS specimen with its new geometry, which prevents plastic deformation and rotation of the supports, has been discussed in [1]. The deformed layer of the MDS specimen has 2 mm and it initially assures the uniform deformation over the gage length at low nominal strain rates. The MDS specimens are loaded by direct impact using a bar projectile, as it is shown in Fig. 5. The scheme of loading by direct impact permits for greater flexibility in programming of the nominal strain rate in shear, simply by changing the impact velocity. The rise-time with this type of loading is practically eliminated in comparison, for example, to SHTB technique. The flat-ended projectiles of different lengths, and diameter $d_p = 10$ mm, are launched from an air gun with predetermined velocities V_i ; $1 \text{ m/s} \leq V_i \leq 200 \text{ m/s}$. The impact velocity V_i is measured by three sources of light 1, fiber optics 3, three independent photodiodes 2 and two time counters 4. Axial displacement $U_x(t)$ of the central part of the MDS specimen is measured as a function of time by an optical, non-contact, displacement transducer 8. In addition, the axial displacement of the specimen-projectile contact is measured at the same time by the second channel of the optical transducer 8. The optical transducer reacts to the axial movements of a small black and white target cemented to the central part of the MDS specimen, channel 1. Since the impact end of the projectile is black, the displacement of the contact between the projectile and MDS specimen is measured in the same way, channel 2.

The axial force transmitted by the specimen symmetric supports can be determined as a function of time from the transmitted longitudinal elastic wave $\varepsilon_T(t)$ measured by strain gages 7, DC supply units 11 and amplifier 10. All electric signals, that is voltages of displacement $V_x(t)$ and $V_c(t)$ and transmitted wave $\varepsilon_T(t)$ are recorded by a digital oscilloscope 12 and stored later in the computer hard disc 13 for further analyses. After analyses of the recorded signals and elimination of time, a force-displacement curve can be constructed for the MDS specimen and $\tau(\Gamma)$ and $\dot{\Gamma}(\Gamma)$ finally determined, where τ and Γ are respectively the shear stress and shear strain, t is time and $\dot{\Gamma} = d\Gamma / dt$. The complete theory of this test is published elsewhere, [4].

The experimental technique based on the MDS specimen and direct impact has appeared to be quite effective for materials testing at high strain rates in shear, $10^3 \text{ s}^{-1} \leq \dot{\Gamma} \leq 10^5 \text{ s}^{-1}$. Typical oscillogram of such test is shown in Fig. 6. The MDS specimen made of VAR 4340 steel, ~52 HRC (standard geometry) was loaded by projectile $L_p = 200 \text{ mm}$ at impact velocity $V_i = 72.3 \text{ m/s}$. The two channel digital oscilloscope with the sampling rate 1 GHz was triggered by the signal from the optical transducer, channel 1. It is visible that the velocity of the central part of the MDS specimen is almost constant, no vibrations are present. The theoretical time of contact is $t_c = 2L_p / C_0$ where C_0 is the elastic wave speed in bar, $C_0 \approx 5.0 \text{ mm} / \mu\text{s}$, finally $t_c = 80 \mu\text{s}$, the time interval much longer in comparison to the rupture time of this specimen $t_f \approx 14.0 \mu\text{s}$. The transmitted wave is recorded by channel 2. The delay to propagate the elastic longitudinal wave in the Hopkinson tube, from specimen to the strain gage is $t_d \approx 37.2 \mu\text{s}$. A special computer program has been developed to analyse the oscillograms and to determine $\tau(\Gamma)$ and $\dot{\Gamma}(\Gamma)$ curves.

Experiments on MDS Specimen With Different Stress Concentrators, VAR 4340 Steel

The main interest was to study further the effect of stress concentrators on formation of ASBs at different rates of loading. The external geometry of the MDS specimen was kept unchanged and only the shear parts were modified. Four geometries were applied as it is shown in Fig. 7, that is the standard geometry, Fig. 7a, the U-geometry, Fig. 7b, the V-geometry, Fig. 7c and the fine notch geometry, Fig. 7d. The ligament a as well as the thickness b were the same for all geometries, $a = 5 \text{ mm}$, $b = 6.0 \text{ mm}$, with exception of the fine notch geometry with $a \approx 5.5 \text{ mm}$. Dimension of this notch, cut by the electro-sparking technique, was $\sim 0.2 \text{ mm}$. The specimens were cut from the second part of the cross-rolled plate of VAR 4340 steel supplied earlier by the ARO-Watertown. The first part was used for a preliminary series of tests reported in [1]. The chemical composition of this plate was :

C – 0.42 (wt. %)

W – 1.74

Cr – 0.89

Mn – 0.46

Si – 0.28

S – 0.001

P – 0.009

All together 91 MDS specimens were produced. Dimensions of specimen for each series, from A to D, geometries from standard to fine notch (Figs. from 7a to 7d), are given in Tables from 1 to 4. All specimens were thermally treated : austenitization 1 hour 925°C and oil quenched, re-austenitized 15 min at 845°C and oil quenched, finally tempered at 200°C - 2 hours. After such thermal treatment the Rockwell Hardness was 52-53 HRC.

The MDS specimens of all four geometries, from A to D, were tested at wide range of the nominal strain rates, from $5 \cdot 10^{-4} \text{ s}^{-1}$ to $\sim 3 \cdot 10^4 \text{ s}^{-1}$. Two types of loading were applied. In order to perform quasi-static tests and also tests with higher strain rates, of the order of 10^3 s^{-1} , a special loading device has been used, [1]. This device is equipped with own measuring systems. The axial force is measured by SR-gages and a signal conditioner, displacement is determined by two precise LVDTs and amplifier. The device was used together with a fast, hydraulic, closed loop, universal testing machine available in LPMM. The signals $F(t)$, that is the force, and LVDT displacement $\delta_1(t)$, $\delta_2(t)$ were recorded by a digital oscilloscope and next stored in a PC hard disk for further analyses. After such tests the shear stress and shear strain can be obtained as a function of time. After elimination of time the $\tau(\Gamma_n)$ curves can be determined, [1]. The second type of loading was by direct impact, the experimental technique is shown in Fig. 5. The following characteristic points have been determined from all quasi-static and dynamic tests: the maximum shear stress τ_m and the nominal strain Γ_m at this maximum, the rupture shear stress τ_c and the nominal strain Γ_c at this stress. For each nominal strain rate two tests were performed and shear strain τ vs the nominal shear strain Γ_n were found. In addition the strain rate history, $\Gamma(\dot{\Gamma})$, was also found. Typical results for the standard MDS geometry are shown in Fig. 8 and Fig. 9. Fig. 8 shows the test results at low strain rate, the mean value $\dot{\Gamma} \approx 5 \cdot 10^{-3} \text{ s}^{-1}$. The dotted curve shows the current strain rate during the test. Fig. 9 shows the tests result at high strain rate $\dot{\Gamma} = 2.8 \cdot 10^4 \text{ s}^{-1}$, obtained with the technique of direct impact, [4]. Comparison of those curves indicates for the relatively reduced rate sensitivity of the yield and flow stress. On the other hand, at the high strain rate, the plasticity is substantially reduced and a quasi-brittle behavior dominates. Of course, this is caused by adiabatic coupling and stress concentrations around the corners of the standard MPD geometry, [1]. This behavior indicates that the specimens of the VAR 4340 steel of this series are overall more brittle in comparison to the preliminary series of tests reported in [1].

The final results for all four specimen geometries, from A to D, and for all spectrum of strain rates, are reported in tables from Tab. 5 to Tab. 8. The following quantities have been determined for each test: the mean strain rate $\dot{\Gamma}$ [1/s], the imposed velocity V_i [m/s], the maximum shear stress τ_m [MPa], the shear strain at τ_m , that is Γ_m , the rupture stress τ_c and the shear strain at τ_c , that is Γ_c . All test results are also shown in the form of graphs from Fig. 10 to Fig. 13, respectively for the standard, "U", "V" and "fine-notch" geometries. The last one is called "S"-geometry.

Because of reduced plasticity the rate sensitivity of shear stress is also reduced, which is visible in Fig. 10 for the standard geometry. The mean values of the rupture stress is from 600 MPa at low strain rates to 900 MPa at strain rate $\sim 5 \cdot 10^4 \text{ s}^{-1}$. The mean rupture strain Γ_c increases within the region of smaller strain rates from ~ 0.018 at $\dot{\Gamma} = 6 \cdot 10^{-4} \text{ s}^{-1}$ up to $\tau_c \approx 0.03$ at $\dot{\Gamma} = 1.0 \text{ s}^{-1}$, and next diminishes substantially to the level ~ 0.01 at $\dot{\Gamma} = 10^4 \text{ s}^{-1}$. This effect is due to occurrence of adiabatic heating and formation of ASBs. It must be mentioned, however, that overall the fracture behavior dominates at this level of hardness (52 \div 53 HRC). A similar behavior is found for the U-geometry, Fig. 11. But the transition from isothermal to adiabatic regimes at $\dot{\Gamma} = 1.0 \text{ s}^{-1}$ is more abrupt.

Geometries V and S (fine notch) behave as almost brittle, and the transition from isothermal to adiabatic regimes are bearly visible. The mean value of fracture stress is about 800 MPa for both cases. Reduced volumes of plastic zones around the notch tips reduce the nominal fracture deformation determined at low strain rates by LVTDS. In conclusion, at this level of hardness the level of brittleness obscures the typical behavior caused by thermally-coupled plasticity. It is well known that stress concentrators supress the volume of plastic zones. The smallest volume occurs for an ideal sharp crack in MODE II, for example [8].

The transition from isothermal to adiabatic regimes of fracturing is more clear when the plastic energy to fracture is analysed as a function of the logarithm of strain rate. Figures from Fig. 14 to Fig. 17 show the plastic fracture energies respectively for the test series from A to D. Within the domain of small strain rates the energy increases at increasing strain rates, this is the case of standard and U-geometries. The maximum level is about 18 MJ to 19 MJ for the standard and U-geometries. The transition to the adiabatic regime is more abrupt for the U-geometry and at high strain rates the plastic energy to fracture is almost zero. Such behavior is caused rather by stress concentrators and a local adiabatic instability, and not by, for example, the CIV in shear, usually, observed for a more ductile metal. The stress concentrators trigger fracture-like processes at loading rates lower than the CIV in shear. Behavior of V- and S-geometries is similar. At low strain rates the mean plastic energy to fracture is around 5 MJ for both geometries, V and S (test series C and D). At high strain rates the energies drop again to a very low level.

The energy analyses resemble very closely the ductile-brittle transition observed in fracture mechanics for an isolated crack when the loading rates are increased from quasi-static to impact. Such behavior was reported in [9] for 1045 steel.

A general conclusion emerging after all series of tests on VAR 4340 steel (52-53 HRC) with different stress concentrators is that at high loading rates this steel is much more prone to fracture than in the quasi-static conditions. Relatively high hardness reduces substantially the plasticity and behavior is closer to fracture mechanics with an adiabatic process zone, for example [10]. This behavior contrasts with previous

preliminary experiments on VAR 4340 steel, with a slightly reduced hardness (50 ÷ 52 HRC), reported in [1]. In this later case a high rate sensitivity of the maximum shear stress was observed and the CIV in shear has been determined around 130 m/s. On the other hand, a relatively small variations of hardness can change behavior of the standard MDS specimen and perhaps, as well, the role of stress concentrators.

Preliminary FE Analysis of the "U" and "V" Geometries *

The three-dimensionnal FE analyses presented here model both the spatial distribution of strain and temperature in MDS specimens with "U" and "V" geometries. Analyses were performed for five levels of the nominal strain, that is $\Gamma_n = \Delta x / h_s$, with $h_s = 2.0$ mm: $\Gamma_n = 0.04 ; 0.08 ; 0.12 ; 0.16$ and 0.20 . The analyses were repeated for three nominal strain rates $\dot{\Gamma} = V_i / h_s$, that is $\dot{\Gamma}_n = 0.1 \text{ s}^{-1} ; 10.0 \text{ s}^{-1}$ and 1000 s^{-1} . The nominal strain rates were obtained with the following imposed velocities: $V_i = 2 * 10^{-4} \text{ m/s} ; 2 * 10^{-2} \text{ m/s}$ and 2.0 m/s . Constitutive relation used in those preliminary analyses was assumed as follows

$$\sigma = \sigma_0 \varepsilon_p^n \left[1 + B(T) \dot{\varepsilon}^{p/(T)} \right] \quad (1)$$

where σ_0 is the quasi-static yield stress in tension-compression, n is the strain hardening exponent, B and p are two material constants which are temperature dependent. Normally $B(\Gamma)$ is an increasing function of the absolute temperature T and $p(T)$ is decreasing when temperature increases. That means that the rate sensitivity $m(T) = 1/p(T)$ is an increasing function of temperature. The constants were fitted to model VAR 4340 steel. The isotropic Huber-Mises flow rule has been assumed in calculations. The problem was treated with the heat conduction. The final deformation and temperature fields for $\Gamma_n = 0.20$ are shown for the U-geometry in figures from Fig. 18 to Fig. 20. The results for the same conditions and for V-geometry are shown in figures from Fig. 21 to Fig. 23. In every case Fig. (a) shows the deformation field (the shear component) and Fig. (b) the temperature field in Kelvins. The figures are referred to the symmetry plane of the specimen.

Concerning the U-geometry the deformation fields are quite similar for three strain rates studied, but the temperature fields show substantial differences. At the highest strain rate ($\dot{\Gamma}_n = 10^3 \text{ s}^{-1}$) the highest mean increase of the temperature in the central part of the

* These numerical analyses were performed by Dr O. Oussouaddi.

cross section is $\Delta\Gamma \approx 73.5$ K. The temperature increments at lower strain rates are much smaller.

Concerning the V-geometry the deformation fields are concentrated near the vicinity of the notch tip. The maximum shear deformations are locally much higher as compared to the U-geometry. At the highest strain rate ($\dot{\Gamma}_n = 10^3$ s⁻¹) the highest increases of temperature are in the vicinity of the notch tip. The increment is substantial, $\Delta T \approx 375$ K. It is expected in conclusion that behavior of the V-notched MDS specimens should be different in comparison to the U-geometry specimens. This preliminary numerical analysis confirms the differences observed in experiments in transition from the isothermal to adiabatic regimes of deformation for both geometries. The summary of the FE results is shown in Fig. 24 for the U-geometry and in Fig. 25 for the V-geometry. The evolution of maximum values of shear strain and temperature as a function of the nominal strain $\Gamma_n = \Delta x / h_s$ confirms the physical intuition, the U-geometry produces much lower strain concentrations and consequently the temperature increments are lower. At higher strain rates the distribution of shear strain is more uniform (the maximum of local strains are lower). On the contrary, the V-geometry produces high local deformations and temperatures in the vicinity of the notch tip and consequently very high gradients of strain and temperatures occur in the shear plane. The instantaneous increase of strain and temperature near the vicinity of the V-notch accelerates the reduction of energy expended for fracture via the local formation of an ASB.

FE Analysis of the Critical Impact Velocity in Shear, Technical Details

A fundamental study has been undertaken to analyse numerically the main factors which trigger the Critical Impact Velocity (CIV) in shear. The study is focussed on VAR 4340 steel, 50-52 HRC, which exhibits limited plasticity. Occurrence of the CIV in shear for this steel has been confirmed experimentally, [1]. Since the analyses based on the concept of the steady-state shearing, [2, 3], do not provide complete information on instability and localization processes when the initial boundary conditions are more realistic, it was decided to define precisely how the velocity is imposed at the begining of the shearing. Thus, to assure occurrence of strain gradients and instabilities caused by inertia, the elastic-plastic wave propagation in shear has been accounted for in the FE analysis.

Finally, the geometry of the deformed layer was assumed the same as previously studied by the steady-state approach, [3]. The layer had a sinusoidal imperfection of

geometry 1% along the height $h_s = 2.0$ mm of the layer. The height is exactly the same as in the MDS geometry.

A very detailed description of the whole project is attached to this Report in the form of Appendix N°1, [11]. An improved version of this study, with more data, can also be found in [12]. Here only the main results are provided.

The infinite layer analysed, depicted in Fig. 26, was charged on the top by the imposed velocity V_i with a specific rise-time. The bottom was completely fixed. In fact, only a part of the infinite layer was modeled, that is 0.5 mm along the direction of impact (x-direction). The geometry imperfection was assumed in the form of sinusoid

$$\omega(y) = \omega_0 \left[1 + \delta_\omega \sin\left(\frac{\Pi}{2} - 2\Pi \frac{y}{h}\right) \right] \quad (2)$$

where $\delta_\omega = 0.005$ is the geometry parameter, and ω_0 is the mean width of the layer, Fig. 26, [3, 11]. All numerical analyses were performed by the FE codes ABAQUS/Standard and ABAQUS/Explicit. The technical details of the FE calculations are given in the Appendix 1 to this Report, [11]. The state of plane strain of the layer was assumed in all calculations. Taking into account the fact of two expected shearing modes; that is "quasi-static" with the strain localization in the middle and "dynamic" with localization at the top, two kinds of meshing were used for 2D simulations, Fig. 27 and Fig. 28. Similar meshes for the 3D simulations, but with smaller number of elements, are given in [11]. Comparison of numerical results for $V_i = 20$ m/s obtained in the form of $\tau_A(\Gamma_n)$ at $y = 0$ (top of the layer), where τ_A is the shear stress determined at $y = 0$, and Γ_n is defined as $\Gamma_n = V_i / h_s$, gave a good agreement between two models, [11].

Depending on the imposed velocity V_i at $y = 0$, the problem was considered either with heat conduction or adiabatic. In the analysis with the heat conduction (fully coupled temperature problem) the inertia effects are neglected (no plastic waves). On the other hand, the analyses with wave effects are assumed adiabatic.

The principal parameter in this study is the imposed velocity V_i at $y = 0$. The velocity V_i was increased by 8 steps from $V_{il} = 2 * 10^{-5}$ m/s ($\dot{\Gamma}_n = 10^{-2}$ s⁻¹) up to 160 m/s ($\dot{\Gamma}_n = 8 * 10^4$ s⁻¹), more details are given in [11]. A more advanced analysis with 17 steps and application of the ABAQUS/Explicit scheme is reported in [12].

Shear velocity $V_i(t)$ at $y = 0$ was applied in the specific way from value of zero to maximum V_{im} . The total rise-time t_m was chosen according to the Gaussian cumulative distribution function. The mathematical form of the rise-time function is given by the following equation

$$F(t) = \int_{t_{\min}}^{t_m} \frac{1}{\sqrt{2\pi\sigma^2}}(X) \left(-\frac{(X-m)^2}{2\sigma^2} \right) dX \quad (3)$$

with $t_{\min} = 0$. Schematic representation of the rise-time function is shown in Fig. 29. Values of the rise-time were assumed as follows : $t_m = 10^{-2}$ s for $V < 1$ m/s, $t_m = 10^{-6}$ s for 1 m/s $\leq V_i \leq 20$ m/s and $t_m = 10^{-7}$ s for $V_i \geq 20$ m/s. Values of constants in eq. (3) are $m = 0.5$ and $\sigma = 0.125$.

In the FE codes available on the market the constitutive relations are usually quite simple and not specifically tailored to particular problems. All problems of plastic instabilities including thermal coupling must be analysed with a precise and reliable constitutive relation or relations. A model chosen reflects later the results. In order to approximate adiabatic instabilities, localization and wave effects, constitutive relations must include strain hardening, rate sensitivity and temperature sensitivity of the flow stress within a wide range of strains, strain rates and temperatures. After careful analyses of experimental data available in the open literature for VAR 4340 steel, ~ 52 HRC, the following explicit form of the constitutive relation has been worked out

$$\tau = \frac{\mu(T)}{\mu_0} \left[B \left(\frac{T}{T_0} \right)^{-v} \left(\Gamma_0 + \Gamma_p \right)^n + \tau_0 \left(1 - \frac{T}{D} \log \frac{\Gamma_0}{\dot{\Gamma}} \right)^m \right] \quad (4)$$

where B , μ_0 , v , n , m are respectively, the modulus of plasticity, the shear modulus at $T = 300$ K, the temperature index, the strain hardening exponent and the logarithmic rate sensitivity, T_0 , Γ_0 , $\dot{\Gamma}$ and D are normalization constants. The temperature change of the shear modulus is given by

$$\mu(T) = \mu_0 \left(1 - AT^* - CT^{*2} \right); T^* = T - 300 \quad (5)$$

where A and B are constants, and $T^* = T - 300$ K is the modified temperature. In principle, this version of constitutive equations can be applied at RT and temperatures above 300 K.

At the begining a simplified version of the constitutive relation (4) was used in the preliminary FE calculations. In this approach the strain hardening exponent n was assumed as a constant. It appeared that the process of localization is unrealistically extended into large strains because of a strong parabolic hardening. It is known, however, that the rate of strain hardening in steels is temperature dependent and it diminishes with an increase of temperature [13]. In the second approach n was assumed as a linearly decreasing function of the homologous temperature, [13]

$$n(T) = n_0 \left(1 - \frac{T}{T_m} \right) \quad (6)$$

where n_0 is the strain hardening exponent at $T = 300$ K, and T_m is the melting point. This modification was found essential for VAR 4340 steel.

The structure of the constitutive relation, eq. (4), has some elements based on the materials science approach. First of all the level of stress is normalised by $\mu(T)/\mu_0$ which takes into account the thermal softening of the crystalline lattice. The first expression in the brackets is simply the internal stress and the second one is the rate and temperature-dependent effective stress, [14].

The procedure of how the constitutive relations have been developed is described with details in Appendix 1 to this Report, [11]. In order to better illustrate the constitutive relation used, the constitutive surface is presented in Fig. 30 in 3D as the shear yield stress in function of absolute temperature and logarithm of shear strain rate.

Total number of constants in eqs (4), (5) and (6) is 12 and they are given in [11]. Majority of results of numerical simulations were obtained with the modified version of the constitutive relation with $n(T)$, however, some results with the constant value of n were also produced, mainly, in order to make comparison of the FE results where both relations are used. Complete FE results are reported elsewhere [11] in this Report only the most important results are discussed. It should be noted that modification of the constitutive relation by $n(T)$ changes only certain temperature-dependent terms in eq. (4), for instance both constitutive relations have identical strain rate sensitivity.

The FE calculations have been carried out with the thermal coupling. Since a large part of the plastic work is converted into heat the temperature of a material increases when plastic deformation advances. The balance of energy with the heat conduction leads to the following relation

$$\beta\tau \frac{\partial\Gamma}{\partial t} = \rho C_v \frac{\partial T}{\partial t} - \lambda \frac{\partial^2 T}{\partial y^2} \quad (7)$$

where y is the axis of the heat conduction, β is the coefficient of energy conversion, [11], ρ , C_v and λ are respectively the mass density, the specific heat and the heat conductivity (Fourier constant). When the process is entirely adiabatic, $\lambda = 0$, (no heat conduction) the heating is uniform in an elementary volume. All material constants, the total is 5, are given in Appendix 1 to this Report, [11].

The thermal characteristics which are discussed above permit for numerical simulations of all temperature-coupled problems as purely adiabatic as well as with the heat conduction. The code ABAQUS includes those thermal-coupling problems in the FE procedures.

Results of the FE Simulations

This part of the Report presents the final results obtained from the ABAQUS simulations. The final results reported here were obtained with the ABAQUS/Explicit FE code, [12]. Preliminary results are reported in Appendix 1 to this Report, [11].

Fig. 31 defines position of the analysed cross-sections of the layer, called A and B. The following definitions of different parameters or variables are used in the figures which show the numerical results:

- (i) Nominal shear strain Γ_n , $\Gamma_n = \Delta x_A / h_s$, where Δx_A is the displacement of the top surface (at $y = 0$), and h_s is the height of the layer, $h_s = 2.0$ mm;
- (ii) Plastic shear strain Γ_A is the current shear strain determined in the cross-section A;
- (iii) Plastic shear strain Γ_B is the current shear strain determined in the cross-section B;
- (iv) Critical nominal shear strain Γ_{nc} is the strain which corresponds to the condition $\partial T_A / \partial \Gamma_n = 0$ (maximum stress) and can be determined from the $\tau_A(\Gamma_n)$ curve;
- (v) Shear stress τ_A determined in the cross-section A (at $y = 0$), this quantity is found from experiments with the MDS geometry.

The complete series of calculations was focused on analyses of the instability point as determined by $\partial \tau_A / \partial \Gamma = 0$ and conditions of localization. The main parameter in those calculations was the imposed velocity V_i .

The main conclusion is that in the isothermal conditions of deformation ($V_i = 2 \cdot 10^{-5}$ m/s), in the absence of thermal softening, the instability strain is infinite. When the impact velocity is increased, beginning from $V_i = 0.2$ m/s ($\dot{\Gamma}_n = 100$ s⁻¹) the instability strain is finite, $\Gamma_{nc} = 0.346$. Thus, an increase of the imposed velocity V_i leads to a decrease of the critical strain. The most substantial change in the instability strain Γ_{nc} occurs between velocities $V_i = 115$ m/s and $V_i = 120$ m/s, values of Γ_{nc} are respectively $\Gamma_{nc} = 0.18$ and $\Gamma_{nc} = 0.008$. A similar transition occurs with the localization strain Γ_{nl} at slightly higher values of V_i , that is in between 125 m/s and 130 m/s.

This transition is caused by the CIV in shear. At lower impact velocities, due to geometry imperfection, the localization occurs in the middle of the layer, that is in the cross-section B, whereas at impact velocities higher than 103 m/s localization occurs near the cross-section A. This is demonstrated in Fig. 32 where the displacement fields are shown for two impact velocities: $V_i = 40$ m/s and $V_i = 115$ m/s. The most important is the COMPLETE change in the displacement field, from the “quasi-static” mode to pure

“dynamic” mode. The difference in the shear strain evolution in cross-sections A and B as a function of the nominal strain Γ_n , that is the Marciniaik plots, are shown respectively for $V_i=40$ m/s and $V_i=115$ m/s in Figs 33 and 34. Although the nominal strain rate in Fig. 33 is $\dot{\Gamma}_n = 2 \cdot 10^4 \text{ s}^{-1}$ the evolution of Γ_A and Γ_B is typical for a layer with an imperfection deformed quasi-statically. On the contrary the Marciniaik plot shown in Fig. 34 for $V_i=115$ m/s, $\dot{\Gamma}_n = 5.75 \cdot 10^4 \text{ s}^{-1}$, is completely inversed, the bulk of plastic deformation and localization occurs in the cross-section A, the evolution of plastic deformation in the cross-section B is substantially reduced. It indicates that the impact velocity 115 m/s is very close to the CIV in shear. Comparison of the spatial distributions of the local strain rate at four impact velocities at the assumed end of localization, $\partial\tau/\partial\Gamma_n = -7 \cdot 10^3 \text{ MPa}$, is shown in Fig. 35. At impact velocity $V_i = 130$ m/s practically all plastic deformation is localized at $y=0$ indicating on the wave trapping of plastic shearing. Spatial distributions of temperature for the same set of impact velocities is shown in Fig. 36. It is clear that the maximum increase of temperature in the middle of the shearing zone may be quite high, around 1000 K in the cross-section B for $V_i = 100$ m/s. At higher impact velocities, above the CIV, the local temperatures at the cross-section A may be even higher reaching values close to the melting point. This was confirmed by the SEM for VAR4340 steel [1]. The local strain rates in the cross-section A are also very high, for example for $V_i = 130$ m/s, $\dot{\Gamma} \approx 2 \cdot 10^6 \text{ s}^{-1}$, Fig. 35. It is interesting to note that at high impact velocities, but lower than the CIV, the maxima of strain rate and temperature are shifted off-center. This is probably caused by the plastic wave propagation in the layer interior. Another observation is a slight increase of the critical nominal shear strains Γ_{nc} begining from ~ 40 m/s. This is caused in turn by the competition between two extreme deformation fields shown in Fig. 32. Such behavior is also clear from Fig. 35.

The most important observation is that the $\tau_A(\Gamma_n)$ curves differ substantially at different impact velocities. This is demonstrated in Figs 37 and 38. In the range of lower impact velocities the $\tau_A(\Gamma_n)$ curves reflect a real behavior of material, this is true up to $V_i \sim 40$ m/s, $\dot{\Gamma} \sim 2 \cdot 10^4 \text{ s}^{-1}$. The $\tau_A(\Gamma_n)$ curve determined at this velocity shows characteristic peak of stress at very small strains. In addition, the initial slope in the “elastic” range becomes much steeper than predicted by the shear modulus. This is caused by interaction of plastic waves and adiabatic instability near the cross-section A. When the impact velocities are still higher, the maximum of shear stress occurs at very small nominal strains, Fig. 38.

The slopes $(\partial\tau/\partial\Gamma)_A$ after the stress maxima are negative and they decrease very rapidly when the impact velocities are high enough. This indicates that the CIV is reached. The instability points appear almost instantaneously with more and more shorter process of localization. In Fig. 14 are shown, normalised by μ (the shear modulus), the

initial slopes of the $\tau_A(\Gamma_n)$ curves as a function of imposed velocity V_i . At low velocities the slopes are equal to μ , but at higher loading rates they are much steeper. The normalized slopes depend also on the rise-time.

The sequence of previous figures clearly demonstrates a substantial evolution of shear stress $\tau_A(\Gamma_n)$ determined at $y=0$, when the impact velocity is increased. Such curves can be determined from the MDS tests. The set of all values of Γ_{nc} and Γ_{nl} determined by the FE analysis is shown in Fig. 40 as a function of the impact velocity V_i . The sequence of points indicates for a complicated interplay of thermal coupling and wave processes. Three regions can be recognized, in the first one the ratio of the localization strain Γ_{nl} to the instability strain Γ_{nc} is almost constant. The second region from $V_i = 103$ m/s to $V_i = 130$ m/s is characterized by the beginning of the thermoplastic deformation trapping by plastic waves. Finally, in the third region at impact velocities higher than 130 m/s the trapping is complete and instantaneous instability and localization occurs with a very small localization strain, typically Γ_{nl} is of the order ~0.002.

It is clear that the phenomenon of the CIV is a PROCESS where the transition is not instantaneous. Consequently, the analytic solutions for the CIV, as presented in the first part of this Report, can not provide an exact value of the CIV but only a crude estimation. The CIV estimated for VAR 4340 steel from the FE simulations is ~ 103 m/s, that is the begining of the CIV transition zone.

The CIV in shear has a far reaching consequeces in fragmentation. Experiments performed with MDS specimens made of VAR 4340 steel [1] clearly indicated on a decrease of the fracturing energy when the impact velocity exceeded ~ 130 m/s. In order to estimate the fracture energy by the FE method as a function of the impact velocity, the $\tau_A(\Gamma_n)$ curves have been integrated up to the localization strain Γ_{nl} . The results for all seventeen simulations are shown in Fig. 41. Within the first region the fracture energy increases up to $E = 681$ MJ/m³ for $V_i = 100$ m/s and next, in the second region, a considerable decrease occurs, for impact velocity $V_i = 100$ m/s the energy reaches level ~8 MJ/m³. In the third region the fracture energy stays almost constant on the level from 6 to 8 MJ/m³. Thus, the energy drop is practically hundred times. Different scales should be used to show the energy level for velocities exceeding 130 m/s.

Summary, discussion and final conclusions

This study was focussed on finding the resistance of VAR 4340 steel ~ 52 HPC to formation of Adiabatic Shear Bands (ASB) at different impact velocities including the range of velocities from 100 m/s up to 130 m/s where the Critical Impact Velocity (CIV)

in shear occurs. In order to gather more informations on the role of stress concentrators in formation of the ASBs a series of tests with the modified double shear technique (MDS) has been completed with four specimen geometries. The stress concentrators were charged to be more and more acute, from the standard geometry to the sharp cut by the electro-spark machining. In addition, a series of FE calculations performed for two notch geometries, that is the "U" and "V" geometries, have shown as it is confirmed by fracture dynamics, large deformations, high strain rates and temperatures at the tip of the V notch.

High increments of temperature around the notch tip reduces, to some extend, the brittle fracture, if the hardness is sufficiently high, and promotes a local development of the ASB, which can propagate later with a high speed, [10, 15]. If the hardness is still higher, plastic deformation is almost completely suppressed and there is no adiabatic crack initiation, the fracturing is brittle. On the other side, thermodynamics and thermally activated processes play a decisive role in ductile to brittle transition in fracture mechanics, [9]. It is known that the high rate of loading in all modes of fracture, I, II and III changes the size of the plastic and process zones. For example, an analysis for Mode II reported in [16] shows a substantial reduction of the plastic zone when the loading rate increases. The next stage is the propagation of ASBs and Mode II cracks. Some analyses are available, for example [17, 18]. However, all analytic estimations are limited to relatively simple solutions. A more detailed analyses would be performed with a more complete constitutive relation which includes the state of hardness or the level of strain hardening.

The results of experiments with the four notch geometries are shown in Figs. from Fig. 10 to Fig. 13. For each geometry from 20 to 25 tests have been performed, the total number was 91. The adiabatic heating causes that for all geometries the localization or the nominal shear strains Γ_{nl} at failure decrease at higher imposed velocities V_i . But the sharp notch introduces a quasi-brittle fracture, even at lower loading rates. For VAR 4340 steel, 52 HRC, a sharp notch reduces the failure energy to very small values for all imposed velocities, Fig. 16 and Fig. 17. A substantial drop of the failure energies is observed for the standard and "U" geometries at the threshold of the nominal strain rates $\dot{\Gamma}_n$ from 10 s^{-1} to 30 s^{-1} . At rates higher than the threshold the failure is quasi-brittle for all four geometries. Since the imposed velocities V_i are lower than the CIV for the steel studied the only explanation of this behavior is existence of the stress concentrators. The stress concentrators increase locally the shear strain and temperature reducing at the same time the volume of a material resisting to the imposed load. Although a material may show in a bulk some resistance to fracture and adiabatic shear banding, stress concentrators diminish the VOLUME within which that resistance takes place. Such scenario explains reduction of the failure energy at higher loading rates. This is the case of more brittle steels with a high level of hardness. If a steel exhibits more plasticity the stress concentrators will be "relaxed" and accommodated by the bulk plastic flow. In such

case the failure energy will increase steady by up to the first sign of the CIV and next will drop abruptly, as it is demonstrated in Fig. 41. This was the case of the VAR 4340 steel ~50-52 HRC tested previously, [1].

A clear picture emerges from the scenarios given above. In tempered and normalized alloy steels the most important factor is the level of hardness, [19]. The hardness indicates for ability to plastic deformation. If plasticity is not much inhibited the main failure will be by adiabatic shear banding or the CIV in shear. Whereas, the thermal treatments which produce a higher level of hardness will introduce a high failure sensitivity to stress concentrators at relatively low rates of loading, lower than the CIV in shear. In such cases the fracture toughness should be evaluated in Mode I and II, [16, 19, 20]. It is also well known that steels exhibit the ductile to brittle transition temperature, which is different at different loading rates, [9, 20]. The transition temperature is normally shifted to a higher temperature as the loading rate is increased. Due to this shift in the transition temperature, a more brittle behavior is the most probable for dynamic loading, whereas more ductile behavior is typical for quasi-static loading.

All those effects, that is the stress concentrators, the CIV in shear and the brittle to ductile transition, play an important role in resistance to impact loading and fragmentation. The thermal treatment and the final microstructure are the key factors in the optimization process. Combination of plasticity and a high fracture toughness is difficult to achieve. The tests on VAR 4340 steel, previous one [1], and present, seem to indicate that the transition from the quasi-brittle behavior to failure by ASBs is very sensitive to the level of hardness. The threshold seems to be around 52 HRC for this steel.

REFERENCES

- [1] J.R.Klepaczko, Experimental Investigation of Adiabatic Shear Banding at Different Impact Velocities, Final Technical Report for the ERO of the US Army, Contract N°DAJA45-90-C-0052, LPMM-Metz, (1993).
- [2] J.R.Klepaczko, P.Lipinski and A.Molinari, An analysis of the thermoplastic catastrophic shear in some metals, in : Impact Loading and Dynamic Behavior of Materials, DGM Informationsgesellschaft Verlag, Oberursel, Vol. 2, (1988),
- [3] J.R.Klepaczko and B.Rezaig, A numerical study of adiabatic shear banding in mild steel by dislocation mechanics based constitutive relations, Mech. of Materials, (1996), in print.
- [4] J.R.Klepaczko, An experimental technique for shear testing at high and very high strain rates. The case of mild steel, Int. J. Impact Engng. 15 (1994), 25.
- [5] J.R.Klepaczko, Plastic shearing at high and very high strain rates, Proc. Conf. EURODYMAT 94, J. de Phys., IV, Coll. C8, (1994), C8-35.
- [6] J.R.Klepaczko, Recent progress in testing of materials in impact shearing, in: Dynamic Fracture, Failure and Deformation, PVP-Vol. 300, ASME, NY (1995), 165.
- [7] F.H.Wu and L.B.Freund, Deformation trapping due to thermoplastic instability in one-dimensional wave propagation, J. Mech. Phys. Solids, 32 (1984), 119
- [8] I.V.Varfolomeyev and J.R.Klepaczko, Effect of strain rate on the geometry of the plastic zone near a Mode II crack tip. Parametric analysis, Strength of Materials (Problems Prochnosti), English translation, N° 3, 27 (1995), 138.

- [9] J.R.Klepaczko, Dynamic crack initiation, some experimental methods and modeling, in: Crack Dynamics in Metallic Materials, Springer Verlag, Vienna (1990).
- [10] M.Zhou, A.J.Rosakis and G.Ravichandran, Dynamically Propagating Shear Bands in Impact-Loaded Prenotched Plates, SM Report 94-01, California Inst. of Technology, Pasadena, CA (1995).
- [11] M.Klosak and J.R.Klepaczko, Numerical study of the Critical Impact Velocity in Shear, Appendix N°1 to the Final Technical Report, Contract N68171-95-C-9071, LPMM Metz University, France (1996).
- [12] J.R.Klepaczko and M.Klosak, Numerical study of the critical impact velocity in shear, *J. Mech. Phys. Solids*, (1996), submitted.
- [13] J.R.Klepaczko, A practical stress-strain strain-rate temperature constitutive relation of the power form, *J. Mech. Working Technology*, 15 (1987), 143.
- [14] J.R.Klepaczko, Modeling of Structural evolution at medium and high strain rates, FCC and BCC metals, in : Constitutive relations and Their Physical Basis, Proc. 8th Risø Mater. Symp., Risø (1987), 387.
- [15] A.Needleman and V.Tvergaard, Analysis of a brittle-ductile transition under dynamic shear loading, Proc. Symp. on the Dynamic Failure Mechanics of Modern Materials in Memory of Professor J. Dufty, Pergamon Press, Oxford (1994), 2571.
- [16] I.V.Varfolomeyev and J.R.Klepaczko, Approximate analysis on strain rate effects and behavior of stress and strain fields at the crack tip in Mode II in Metallic Materials, Appendix N°1 to the Technical Report ERO, US Army RDSG, Contract DAYA 45-90-C-0052 (1992).
- [17] D.E.Grady, Properties of an adiabatic shear-band process zone, *J. Mech. Phys. Solids*, 40 (1992), 1197.
- [18] T.W.Wright and J.W.Walter, The asymptotic structure of an adiabatic shear band in antiplane motion, *J. Mech. Phys. Solids*, 44 (1996), 77.

- [19] J.G.Cowie, The Influence of second-phase dispersions on shear instability and fracture toughness of ultrahigh strength 4340 steel, Report N° MTL TR 89-20, US Army Materials Technology Laboratory, Watertown, MA (March 1989).
- [20] Y.C.Chi, S.Lee, K.Cho and J.Dufy, The effects to tempering and test temperature on the dynamic fracture initiation behavior of an AISI 4340 VAR steel, Mat. Sci. and Engng., A114 (1989), 105.

TABLES

- TAB. 1 Dimensions of specimen VAR 4340 steel, series A: standard geometry.
- TAB. 2 Dimensions of specimen VAR 4340 steel, series B: U-geometry.
- TAB. 3 Dimensions of specimen VAR 4340 steel, series C: V-geometry.
- TAB. 4 Dimensions of specimen VAR 4340 steel, series D: fine notch.
- TAB. 5 Test results for VAR 4340 steel, series A: standard geometry, below the thicker line are the direct impact tests.
- TAB. 6 Test results for VAR 4340 steel, series B: U-geometry.
- TAB. 7 Test results for VAR 4340 steel, series C: V-geometry.
- TAB. 8 Test results for VAR 4340 steel, series D: fine notch.

FIGURE CAPTIONS

- Fig. 1 Nominal instability strain, $\Gamma_{nc} = \Delta X/h_s$ and localization strain Γ_{nl} versus nominal strain rate V_i / h_s , [3] ; numerical results for 1018 steel.
- Fig. 2 Changes of temperature within the uniform deformation zone (at layer edges) and in the ASB core, [3] ; numerical results for 1018 steel.
- Fig. 3 Nominal shear strain to fracture for 1018 steel (XC18 steel, French Standard) versus shear strain rate, [1].
- Fig. 4 Energy to fracture for MDS specimen tested at different nominal strain rates, 1018 steel (XC18).
- Fig. 5 Configuration of experimental setup for impact shearing of the MDS specimen.
- Fig. 6 Oscillogram of the test on MDS specimen, VAR 4340 steel, (standard geometry) loaded by projectile, $L_p = 200\text{mm}$, with impact velocity 72.3m/s .
- Fig. 7 Specimen geometries with different stress concentrators.
- Fig. 8 Result of quasi-static test on MDS specimen, VAR 4340 steel, $\dot{\Gamma} \approx 5 * 10^{-4}\text{s}^{-1}$.
- Fig. 9 Test result of direct impact loading, VAR 4340 steel, $\dot{\Gamma} \approx 2.8 * 10^4\text{s}^{-1}$.
- Fig. 10 Strain rate spectrum for the standard geometry (series A), VAR 4340 steel.
- Fig. 11 Strain rate spectrum for the U-geometry (series B), VAR 4340 steel.
- Fig. 12 Strain rate spectrum for the V-geometry (series C), VAR 4340 steel.
- Fig. 13 Strain rate spectrum for the fine notch geometry (series D), VAR 4340 steel.

- Fig. 14 Total energy to fracture for the standard geometry (series A), VAR 4340 steel.
- Fig. 15 Total energy to fracture, U-geometry (series B), VAR 4340 steel.
- Fig. 16 Total energy to fracture, V-geometry (series C), VAR 4340 steel.
- Fig. 17 Total energy to fracture, fine notch geometry (series D), VAR 4340 steel.
- Fig. 18 FE shear deformation and temperature fields for $\Gamma_n = 0.2$ and $\dot{\Gamma}_n = 0.1 \text{ s}^{-1}$, U-geometry.
- Fig. 19 FE shear deformation and temperature fields for $\Gamma_n = 0.2$ and $\dot{\Gamma}_n = 10 \text{ s}^{-1}$, U-geometry.
- Fig. 20 FE shear deformation and temperature fields for $\Gamma_n = 0.2$ and $\dot{\Gamma}_n = 1000 \text{ s}^{-1}$, U-geometry.
- Fig. 21 FE shear deformation and temperature fields for $\Gamma_n = 0.2$ and $\dot{\Gamma}_n = 0.1 \text{ s}^{-1}$, V-geometry.
- Fig. 22 FE shear deformation and temperature fields for $\Gamma_n = 0.2$ and $\dot{\Gamma}_n = 10 \text{ s}^{-1}$, V-geometry.
- Fig. 23 FE shear deformation and temperature fields for $\Gamma_n = 0.2$ and $\dot{\Gamma}_n = 1000 \text{ s}^{-1}$, V-geometry.
- Fig. 24 Evolution of maximum strains and temperatures in the middle of the shear plane, the MDS specimen, V-geometry.
- Fig. 25 Evolution of maximum strains and temperatures in the middle of the shear plane, the MDS specimen, V-geometry.
- Fig. 26 The infinite layer in x-direction with geometry imperfection in the middle.
- Fig. 27 FE mesh applied to simulate plastic localization in the middle of the layer - 2D model.

- Fig. 28 FE mesh applied to simulate plastic localization at the upper surface of the layer - 2D model.
- Fig. 29 Boundary conditions for the imposed velocity V_i at $y = 0$.
- Fig. 30 Constitutive surface for yield stress as a function of temperature and logarithm of strain rate, case of $n = \text{const.}$, VAR 4340 steel, ~ 52 HRC.
- Fig. 31 Definition of the cross-sections A and B.
- Fig. 32 Two displacement fields for two different imposed velocities, (a) $V_i = 40\text{m/s}$; (b) $V_i = 130\text{m/s}$.
- Fig. 33 Marciniak plot showing evolution of shear-strain in cross-sections A and B at $V_i = 40\text{m/s}$; $\dot{\Gamma}_n = 2 * 10^4 \text{s}^{-1}$.
- Fig. 34 Marciniak plot showing evolution of shear-strain in cross-sections A and B at $V_i = 115\text{m/s}$; $\dot{\Gamma}_n = 5,75 * 10^4 \text{s}^{-1}$.
- Fig. 35 Spatial distributions of shear-strain rate for four imposed velocities at the end of localization, $(\partial\Gamma / \partial\Gamma_n) = -7 * 10^3 \text{MPa}$.
- Fig. 36 Spatial distributions of temperatures for four imposed velocities at the end of localization, $(\partial\Gamma / \partial\Gamma_n) = -7 * 10^3 \text{MPa}$.
- Fig. 37 Shear stress Γ_A vs nominal shear-strain Γ_n determined from displacement of cross-section A, imposed velocities lower than the CIV.
- Fig. 38 Shear stress Γ_A versus nominal shear strain Γ_n determined from displacement of cross-section A, impact velocities close to and above the CIV.
- Fig. 39 Nominal slopes of $\Gamma_A(\Gamma)$ curves.
- Fig. 40 Nominal shear strains of instability Γ_{ne} and localization Γ_{nl} as a function of impact velocity V_i .
- Fig. 41 Fracture energy versus impact velocity V_i .

SERIES A

Nº	a1 [mm]	b1 [mm]	a2 [mm]	b2 [mm]	a mean [mm]	b mean [mm]	AREA [mm ²]
1	5,26	6,45	5,38	6,32	5,32	6,39	33,97
2	5,29	6,41	5,42	6,51	5,36	6,46	34,59
3	5,13	6,16	5,06	6,12	5,10	6,14	31,28
4	5,13	6,25	5,22	6,26	5,18	6,26	32,37
5	5,28	6,35	5,42	6,41	5,35	6,38	34,13
6	5,03	6,12	5,15	6,06	5,09	6,09	31,00
7	5,31	6,35	5,20	6,23	5,26	6,29	33,05
8	5,24	6,27	5,33	6,24	5,29	6,26	33,06
9	5,02	6,18	5,14	6,09	5,08	6,14	31,17
10	5,33	6,35	5,36	6,38	5,35	6,37	34,02
11	5,41	6,25	5,24	6,31	5,33	6,28	33,44
12	5,28	6,37	5,38	6,48	5,33	6,43	34,25
13	5,32	6,43	5,19	6,32	5,26	6,38	33,50
14	5,06	6,26	4,93	6,17	5,00	6,22	31,04
15	5,06	6,09	5,15	6,14	5,11	6,12	31,22
16	5,38	6,44	5,27	6,38	5,33	6,41	34,13
17	5,22	6,35	5,34	6,37	5,28	6,36	33,58
18	5,31	6,37	5,39	6,31	5,35	6,34	33,92
19	5,20	6,28	5,32	6,38	5,26	6,33	33,30
20	5,39	6,42	5,26	6,29	5,33	6,36	33,84
21	5,26	6,33	5,36	6,40	5,31	6,37	33,80

TAB. 1

SERIES B

Nº	a1 [mm]	b1 [mm]	a2 [mm]	b2 [mm]	a mean [mm]	b mean [mm]	AREA [mm ²]
1	4,83	6,33	4,85	6,33	4,84	6,33	30,64
2	4,81	6,31	5,01	6,16	4,91	6,24	30,61
3	4,72	5,96	4,77	6,13	4,75	6,05	28,68
4	4,64	6,04	4,63	6,06	4,64	6,05	28,04
5	4,72	6,05	4,93	6,18	4,83	6,12	29,50
6	4,62	6,25	4,60	6,16	4,61	6,21	28,61
7	4,81	6,23	4,96	6,10	4,89	6,17	30,12
8	4,97	6,11	4,89	6,07	4,93	6,09	30,02
9	4,85	6,22	4,88	6,25	4,87	6,24	30,33
10	4,78	6,17	4,87	6,05	4,83	6,11	29,48
11	4,70	6,00	4,82	6,07	4,76	6,04	28,73
12	4,80	6,08	4,84	6,13	4,82	6,11	29,43
13	4,92	6,19	4,86	6,04	4,89	6,12	29,90
14	4,83	6,17	4,65	6,10	4,74	6,14	29,08
15	4,84	6,08	4,90	6,20	4,87	6,14	29,90
16	4,98	6,05	4,88	6,13	4,93	6,09	30,02
17	5,00	6,23	4,82	6,15	4,91	6,19	30,39
18	4,78	6,06	4,86	6,20	4,82	6,13	29,55
19	4,79	6,19	4,84	6,10	4,82	6,15	29,59
20	4,77	5,98	4,96	6,14	4,87	6,06	29,48
21	4,78	6,14	4,88	6,27	4,83	6,21	29,97
22	4,66	6,15	4,83	6,20	4,75	6,18	29,30
23	5,01	6,19	5,02	6,21	5,02	6,20	31,09
24	4,89	6,18	4,63	6,14	4,76	6,16	29,32
25	4,84	6,18	4,70	6,30	4,77	6,24	29,76

TAB. 2

SERIES C

Nº	a1 [mm]	b1 [mm]	a2 [mm]	b2 [mm]	a mean [mm]	b mean [mm]	AREA [mm ²]
1	4,97	6,05	5,17	5,98	5,07	6,02	30,50
2	5,06	6,04	5,08	6,24	5,07	6,14	31,13
3	5,08	6,03	5,17	6,07	5,13	6,05	31,01
4	5,24	6,16	5,35	6,25	5,30	6,21	32,86
5	5,12	6,01	5,15	6,11	5,14	6,06	31,12
6	5,03	6,13	5,12	6,08	5,08	6,11	30,98
7	5,08	6,08	5,11	6,20	5,10	6,14	31,28
8	5,14	6,07	5,09	6,10	5,12	6,09	31,12
9	5,14	6,28	5,12	6,26	5,13	6,27	32,17
10	4,88	6,04	5,00	5,96	4,94	6,00	29,64
11	5,26	5,92	5,02	5,95	5,14	5,94	30,51
12	5,19	6,36	5,08	6,13	5,14	6,25	32,07
13	4,91	6,05	4,98	6,16	4,95	6,11	30,19
14	5,11	6,17	5,14	6,07	5,13	6,12	31,37
15	5,03	6,08	5,02	6,06	5,03	6,07	30,50
16	5,09	6,42	5,01	6,42	5,05	6,42	32,42
17	5,06	6,09	5,01	6,07	5,04	6,08	30,61
18	4,80	6,03	4,68	6,08	4,74	6,06	28,70
19	5,07	6,05	5,17	6,17	5,12	6,11	31,28
20	4,94	6,17	5,05	6,05	5,00	6,11	30,52
21	5,04	6,06	5,04	6,23	5,04	6,15	30,97
22	5,24	6,11	5,18	6,20	5,21	6,16	32,07
23	5,13	6,11	5,07	6,04	5,10	6,08	30,98
24	5,00	6,17	4,98	6,16	4,99	6,17	30,76
25	4,83	6,12	4,98	6,11	4,91	6,12	29,99
26	4,87	6,16	4,82	6,02	4,85	6,09	29,51

TAB. 3

SERIES D

Nº	a1 [mm]	b1 [mm]	a2 [mm]	b2 [mm]	a mean [mm]	b mean [mm]	AREA [mm ²]
1	5,83	6,00	6,16	5,90	6,00	5,95	35,67
2	7,27	6,08	6,56	6,03	6,92	6,06	41,87
3	5,41	6,08	6,67	5,98	6,04	6,03	36,42
4	6,6	6,04	6,22	6,14	6,41	6,09	39,04
5	5,18	6,05	5,33	5,97	5,26	6,01	31,58
6	5,36	6,08	5,35	6,07	5,36	6,08	32,53
7	5,48	6,07	5,39	6,02	5,44	6,05	32,85
8	5,6	5,93	5,25	6,03	5,43	5,98	32,44
9	5,27	6,02	5,15	5,85	5,21	5,94	30,92
10	5,51	5,95	5,12	5,84	5,32	5,90	31,33
11	5,24	6,24	5,62	6,09	5,43	6,17	33,48
12	5,27	6,09	5,44	5,94	5,36	6,02	32,21
13	5,11	5,95	5,24	5,94	5,18	5,95	30,77
14	5,59	6,04	5,07	5,90	5,33	5,97	31,82
15	5,26	6,09	5,28	5,89	5,27	5,99	31,57
16	5,24	6,12	5,30	6,02	5,27	6,07	31,99
17	5,24	6,18	5,19	6,12	5,22	6,15	32,07
18	5,12	6,07	5,11	5,99	5,12	6,03	30,84
19	5,28	6,07	5,36	6,00	5,32	6,04	32,11
20	5,41	5,93	5,41	5,89	5,41	5,91	31,97
21	5,13	5,67	5,32	5,63	5,23	5,65	29,52
22	5,11	6,04	5,31	6,07	5,21	6,06	31,55
23	5,06	6,00	5,09	6,04	5,08	6,02	30,55
24	4,94	6,00	4,82	6,00	4,88	6,00	29,28

TAB. 4

SERIES A

N°	$\dot{\Gamma}$ [1/s]	V_i [m/s]	τ_m [Mpa]	Γ_m	τ_c [Mpa]	Γ_c	E [MJ]
A01	5,970E-04	2,0E-06	657,0	0,012	605,9	0,017	6,53
A02	4,970E-04	2,0E-06	698,0	0,015	661,8	0,019	7,33
A03	4,990E-03	2,0E-05	790,8	0,014	668,4	0,024	11,86
A04	5,670E-03	2,0E-05	757,9	0,017	570,7	0,035	19,69
A05	5,120E-02	2,0E-04	713,3	0,017	701,7	0,018	7,35
A06	5,110E-02	2,0E-04	869,2	0,022	802,4	0,031	17,63
A07	5,180E-01	2,0E-03	746,0	0,029	730,7	0,030	14,38
A08	5,410E-01	2,0E-03	796,4	0,020	780,8	0,026	12,09
A09	3,745E+01	1,8E-01	849,6	0,023	719,5	0,024	13,58
A10	4,376E+01	1,9E-01	696,1	0,019	-	-	11,91
A11	2,542E+01	1,9E-01	747,4	0,018	742,5	0,018	6,06
A12	2,240E+02	2,5E+00	662,7	0,013	642,5	0,015	4,19
A13	2,677E+02	2,5E+00	687,7	0,012	642,1	0,016	5,79
A14	2,220E+03	21,7	722,0	0,009	-	-	0,00
A15	4,970E+03	23,5	484,0	0,006	-	-	0,00
A16	1,400E+04	55,4	773,0	0,011	-	-	0,53
A17	2,420E+04	73,4	850,0	0,012	-	-	1,47
A18	3,540E+04	118,8	875,0	0,012	-	-	1,51
A19	2,800E+04	114,7	981,0	0,014	-	-	2,77

TAB. 5

SERIES B

Nº	Γ [1/s]	V_i [m/s]	τ_m [Mpa]	Γ_m	τ_c [Mpa]	Γ_c	E [MJ]
B01	4,840E-03	2,0E-05	893,3	0,022	887,7	0,023	8,97
B02	5,040E-03	2,0E-05	920,1	0,025	918,0	0,026	12,26
B04	4,930E-02	2,0E-04	1056,0	0,033	-	-	19,51
B05	6,230E-02	2,5E-04	973,2	0,028	972,5	0,028	17,13
B06	6,130E-01	2,5E-03	1027,6	0,033	-	-	20,48
B07	6,360E-01	2,5E-03	920,9	0,032	-	-	18,50
B08	5,138E+00	2,5E-02	927,8	0,022	-	-	9,12
B09	4,414E+00	2,5E-02	855,6	0,014	844,6	0,015	4,15
B10	3,275E+01	2,5E-01	868,1	0,014	-	-	2,07
B11	3,265E+01	2,5E-01	855,4	0,013	842,0	0,014	2,64
B12	3,478E+01	2,5E+00	737,4	0,009	-	-	0,00
B13	3,250E+03	22,7	797,0	0,010	-	-	0,00
B14	2,540E+03	24,2	798,0	0,011	-	-	0,57
B15	1,660E+04	66,5	1031,0	0,014	-	-	2,94
B16	1,880E+04	65,6	1047,0	0,014	-	-	2,93
B17	2,750E+04	115,5	1024,0	0,013	-	-	0,00
B18	2,610E+04	109,9	1087,0	0,016	-	-	4,32

TAB. 6

SERIES C

Nº	Γ [1/s]	V_i [m/s]	τ_m [Mpa]	Γ_m	τ_c [Mpa]	Γ_c	E [MJ]
C01	4,360E-03	2,0E-06	946,1	0,017	894,4	0,021	8,33
C02	4,280E-03	2,0E-06	870,7	0,018	-	-	6,50
C03	4,250E-03	2,0E-05	928,8	0,017	-	-	4,52
C04	3,900E-03	2,0E-05	873,5	0,013	-	-	2,23
C06	4,650E-02	2,0E-04	889,8	0,017	827,2	0,020	8,33
C07	3,990E-02	2,0E-04	850,0	0,014	-	-	2,53
C08	4,370E-01	2,0E-03	886,8	0,018	-	-	5,67
C09	4,390E-01	2,0E-03	878,2	0,019	-	-	6,21
C10	3,119E+01	2,5E-01	861,7	0,012	814,7	0,013	2,73
C11	2,090E+02	2,5E-01	734,2	0,016	627,2	0,018	6,30
C12	3,660E+01	2,5E+00	773,7	0,012	-	-	1,09
C13	3,655E+01	2,5E+00	889,5	0,013	-	-	1,83
C14	3,350E+03	23,6	819,0	0,011	-	-	0,00
C15	2,740E+03	23,6	832,0	0,010	-	-	0,00
C16	1,790E+04	63,5	765,0	0,010	-	-	1,02
C17	1,440E+04	64,8	851,0	0,012	-	-	0,35
C18	2,160E+04	115,5	1049,0	0,015	-	-	3,44
C19	1,890E+04	113,9	871,0	0,011	-	-	0,75

TAB. 7

SERIES D

Nº	Γ [1/s]	V_i [m/s]	τ_m [Mpa]	Γ_m	τ_c [Mpa]	Γ_c	E [MJ]
D02	4,590E-03	2,0E-05	729,7	0,017	-	-	5,26
D03	4,670E-03	2,0E-05	834,0	0,020	-	-	7,39
D04	4,500E-01	2,0E-03	765,6	0,015	760,4	0,016	4,64
D05	4,530E-01	2,0E-03	949,4	0,017	944,7	0,019	6,58
D06	3,803E+00	2,5E-02	798,7	0,012	-	-	1,84
D07	3,243E+00	2,5E-02	871,5	0,013	-	-	1,77
D08	2,690E+01	2,5E-01	720,1	0,011	706,9	0,012	1,76
D09	2,684E+01	2,5E-01	908,2	0,014	-	-	2,23
D10	3,363E+01	2,5E+00	710,7	0,009	-	-	0,00
D13	2,780E+03	23,2	825,0	0,010	-	-	0,00
D17	3,710E+03	23,2	803,0	0,010	-	-	0,29
D18	2,530E+04	65,6	849,0	0,011	-	-	0,83
D19	2,140E+04	67,4	853,0	0,012	-	-	1,37
D21	2,050E+04	111,8	871,0	0,012	-	-	0,93
D23	2,800E+04	114,9	1010,0	0,015	-	-	3,52

TAB. 8

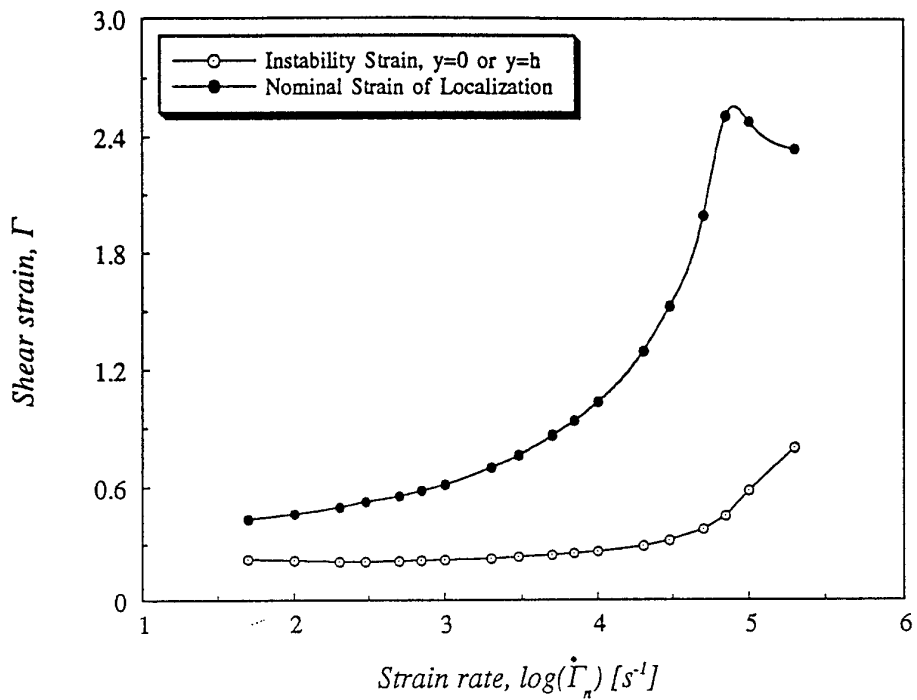


Fig. 1

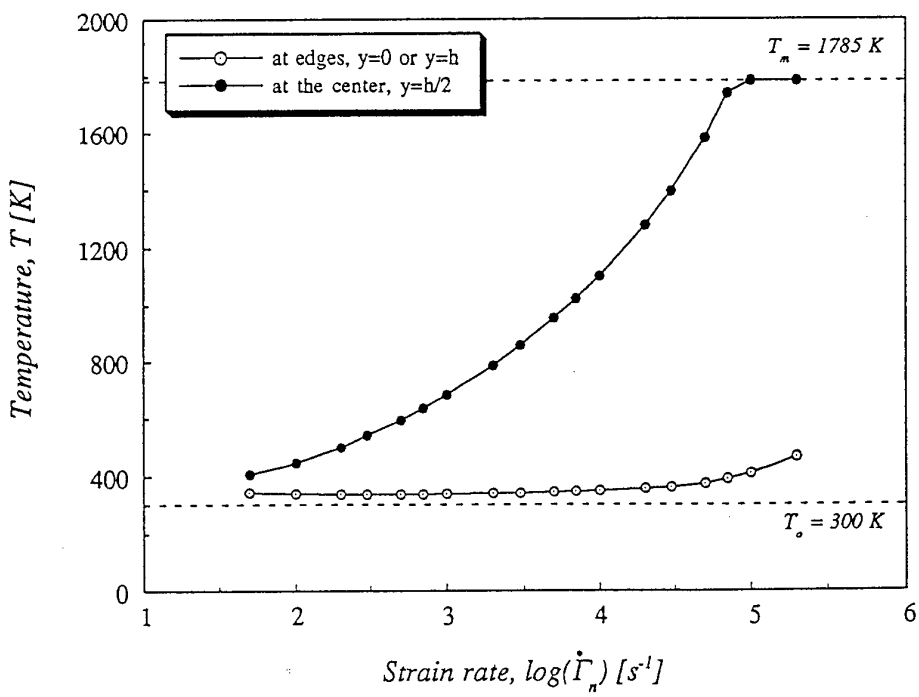


Fig. 2

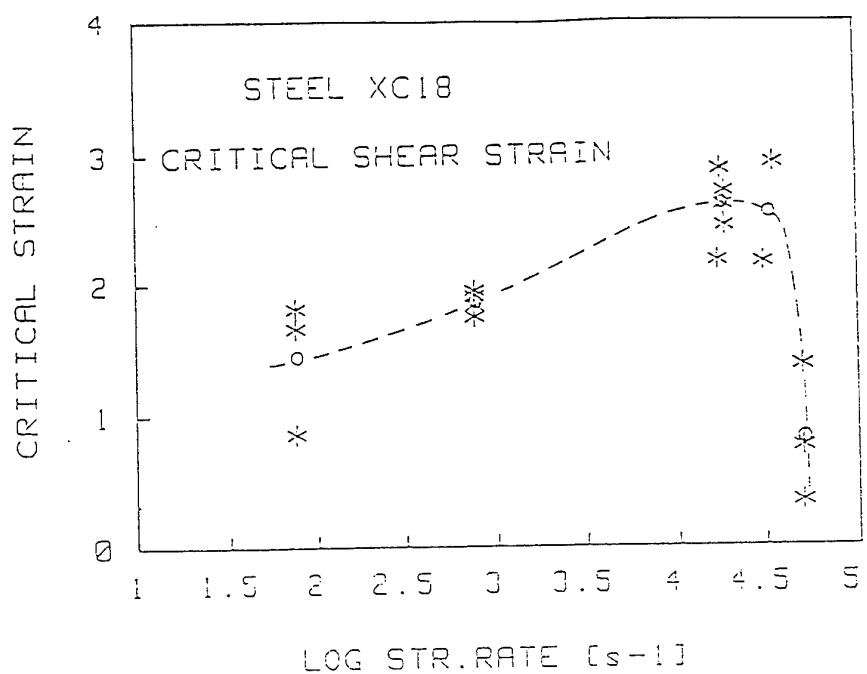


Fig. 3

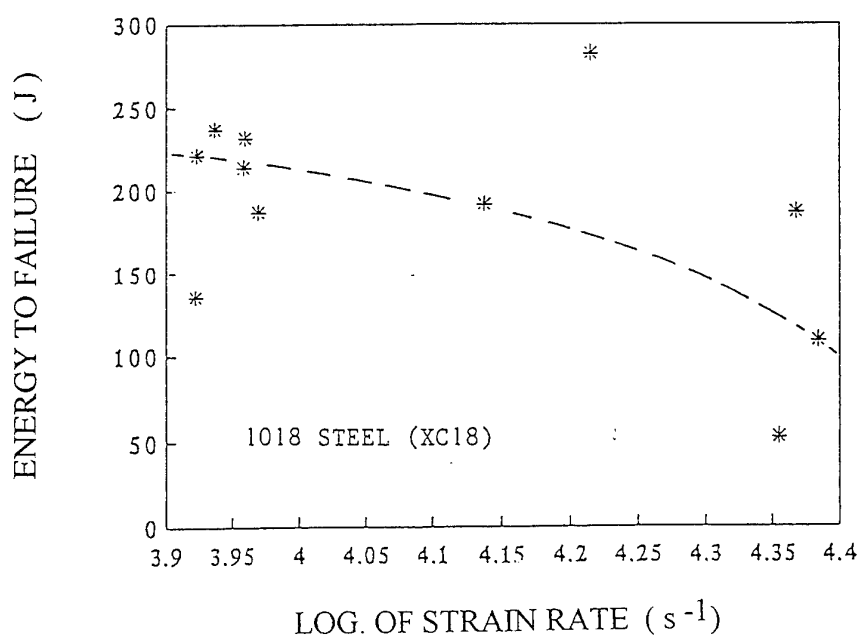
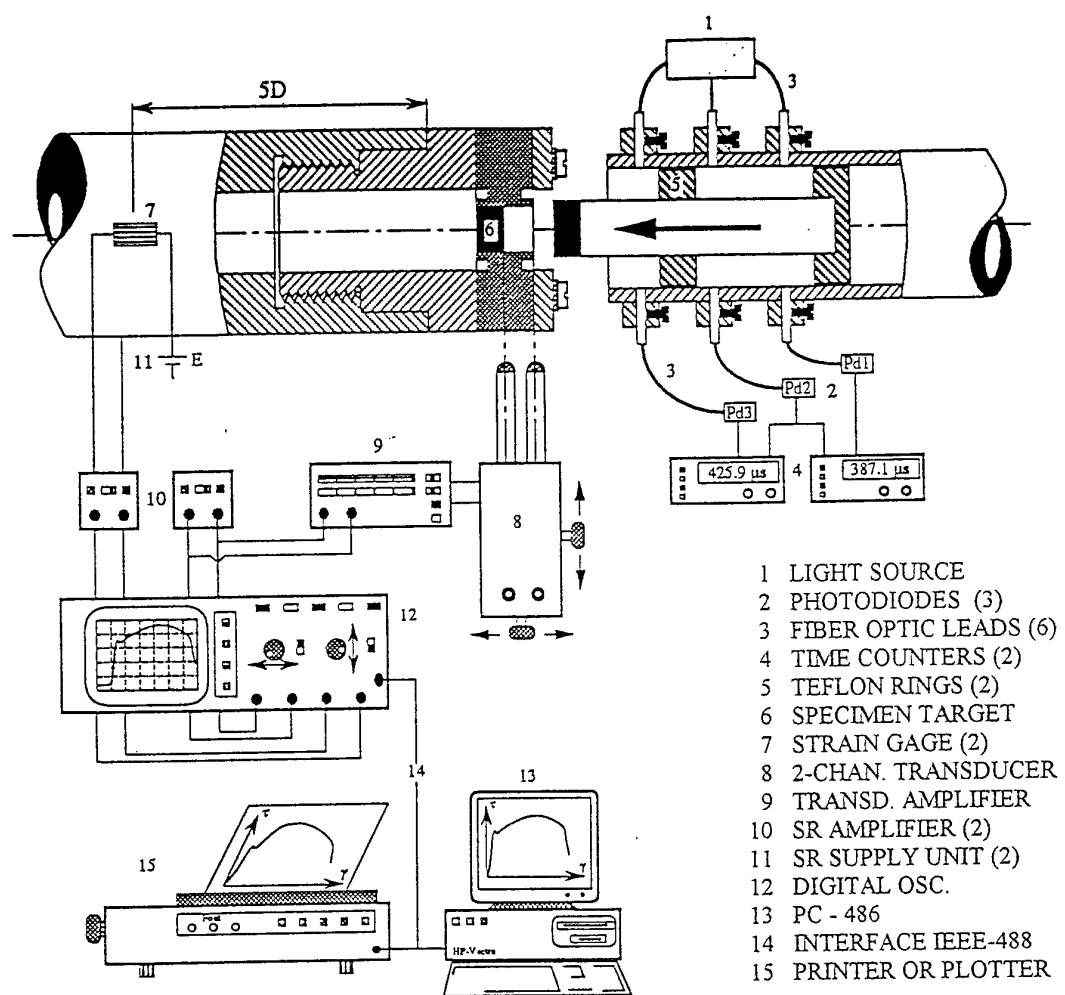


Fig. 4



- 1 LIGHT SOURCE
- 2 PHOTODIODES (3)
- 3 FIBER OPTIC LEADS (6)
- 4 TIME COUNTERS (2)
- 5 TEFILON RINGS (2)
- 6 SPECIMEN TARGET
- 7 STRAIN GAGE (2)
- 8 2-CHAN. TRANSDUCER
- 9 TRANSD. AMPLIFIER
- 10 SR AMPLIFIER (2)
- 11 SR SUPPLY UNIT (2)
- 12 DIGITAL OSC.
- 13 PC - 486
- 14 INTERFACE IEEE-488
- 15 PRINTER OR PLOTTER

Fig. 5

FILES: 17DV3.NGF

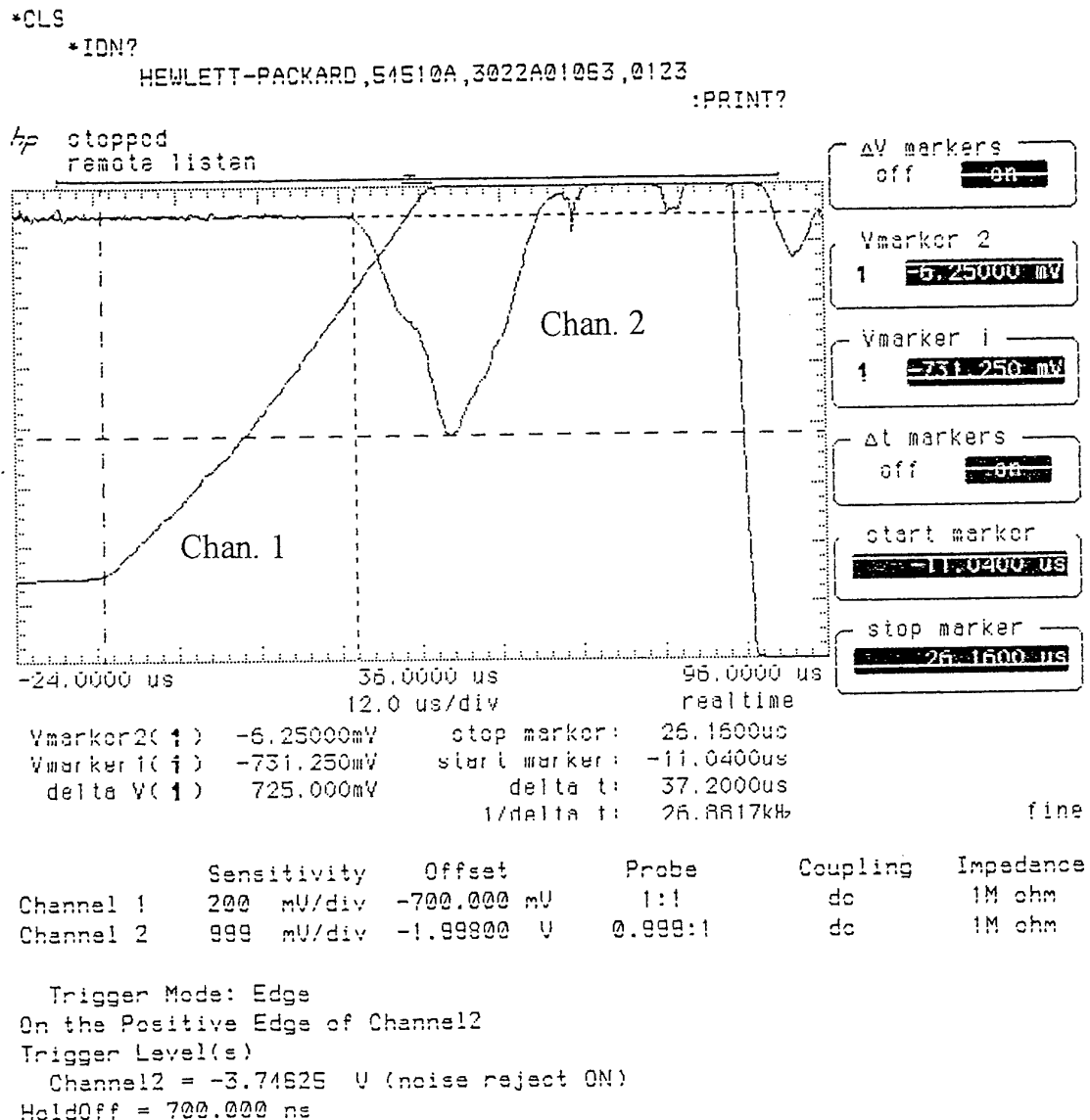
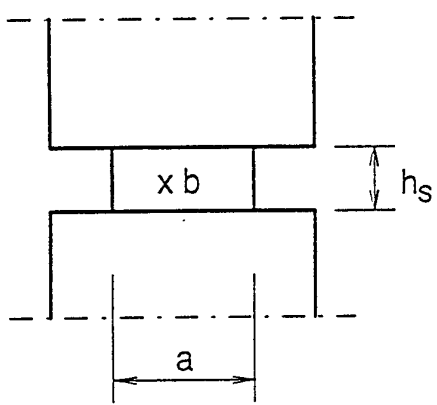
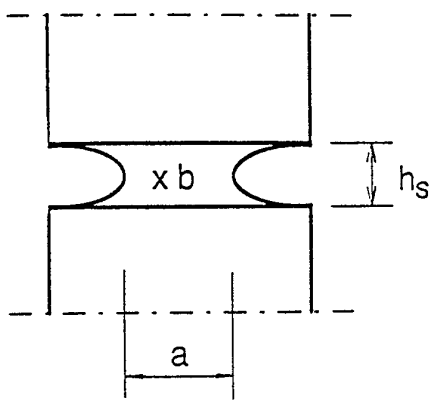


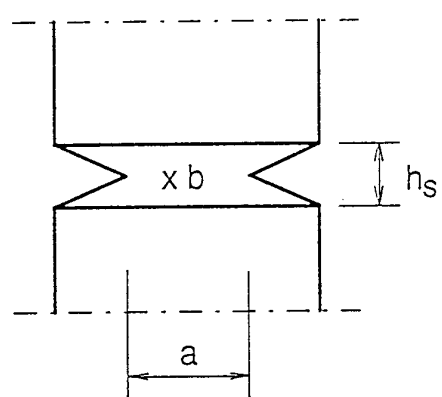
Fig. 6



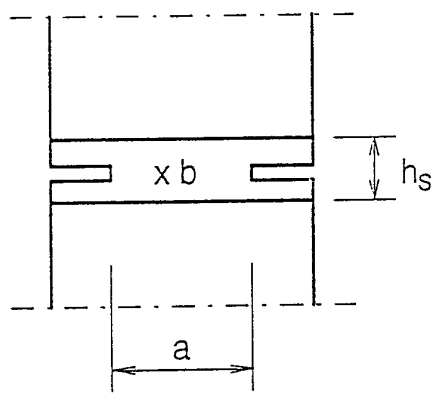
(a)



(b)



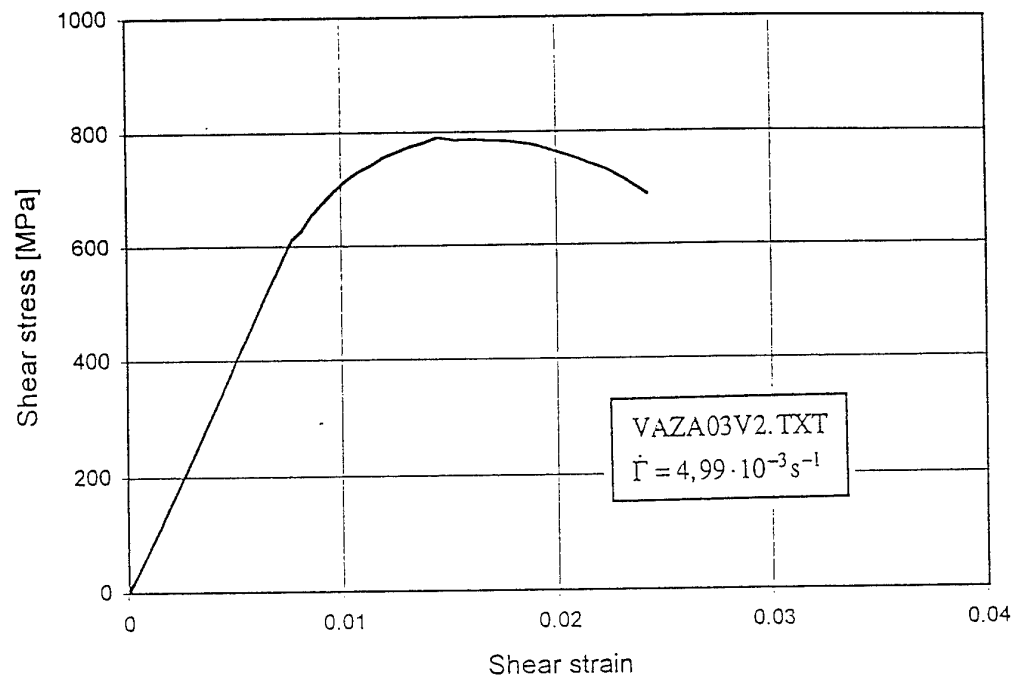
(c)



(d)

Fig. 7

VAR 4340, 52 HRC - STANDARD GEOMETRY



VAR 4340, 52 HRC

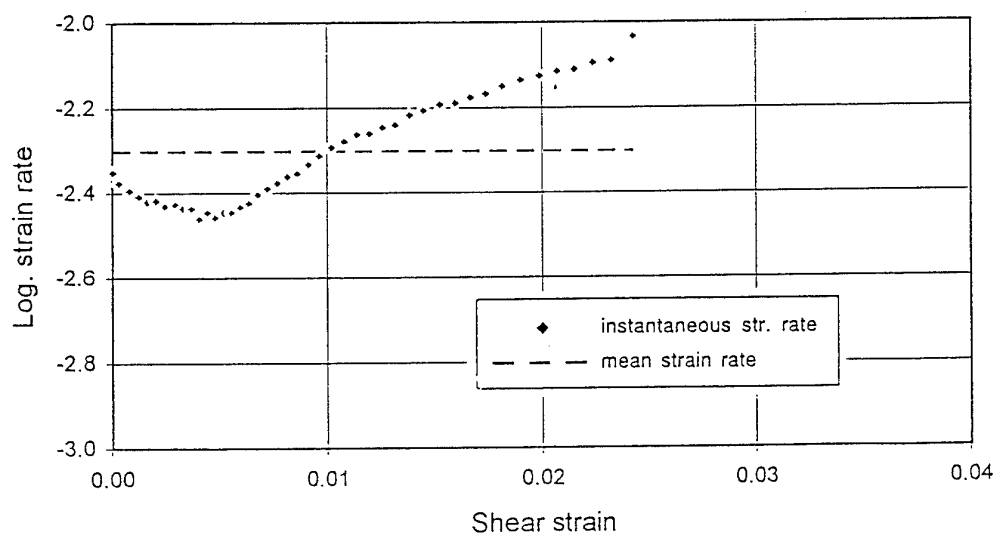


Fig. 8

VAR 4340, 52 HRC - STANDARD GEOMETRY

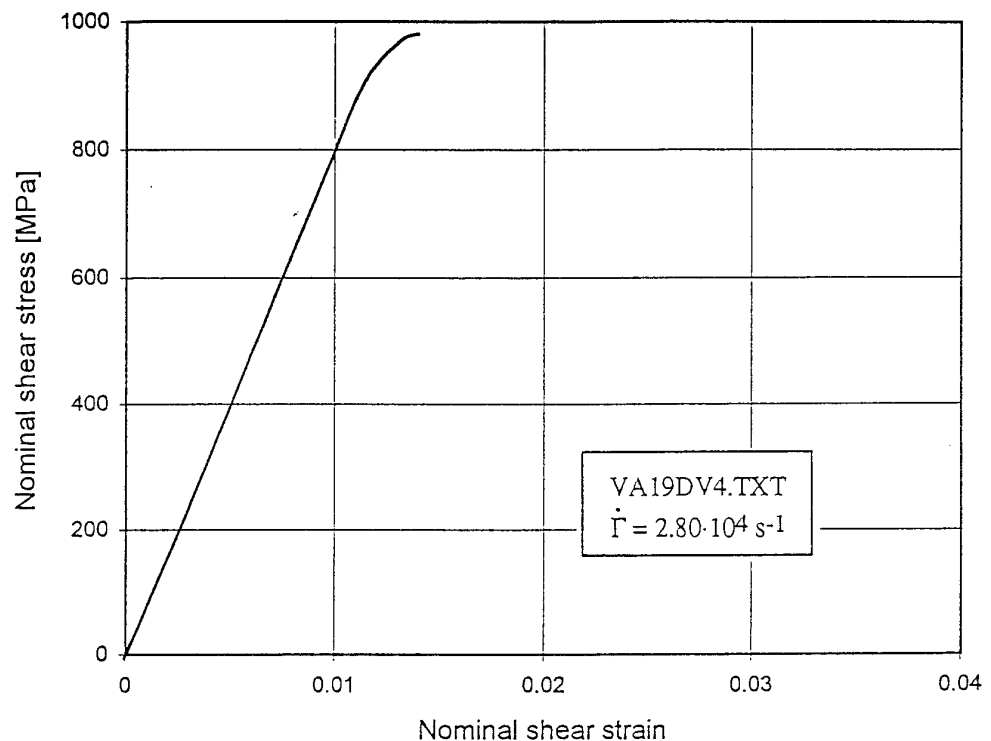
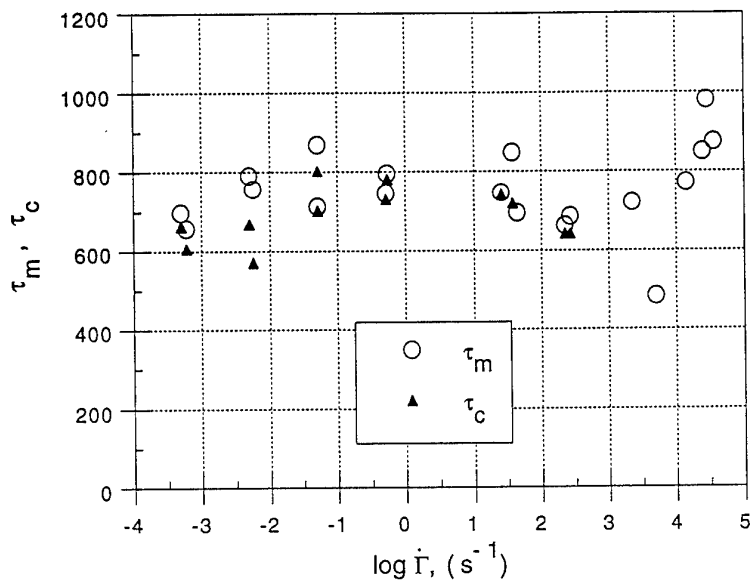


Fig. 9

Standard geometry



Standard geometry

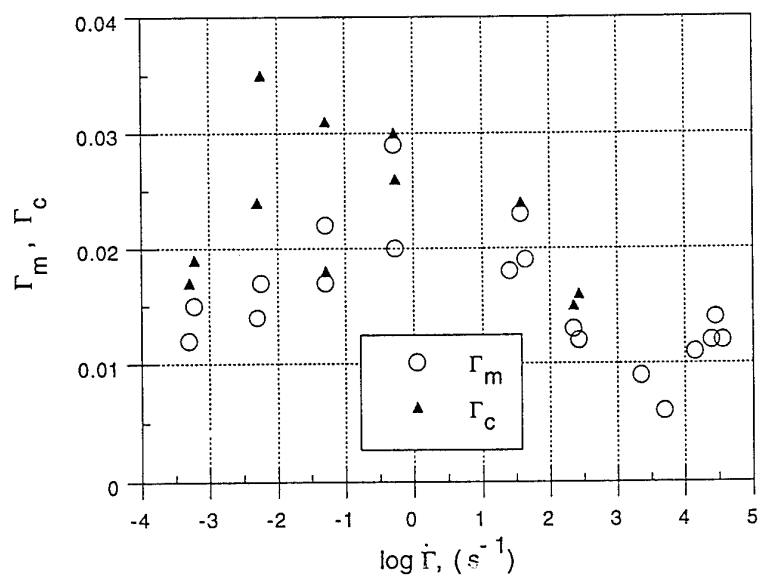


Fig. 10

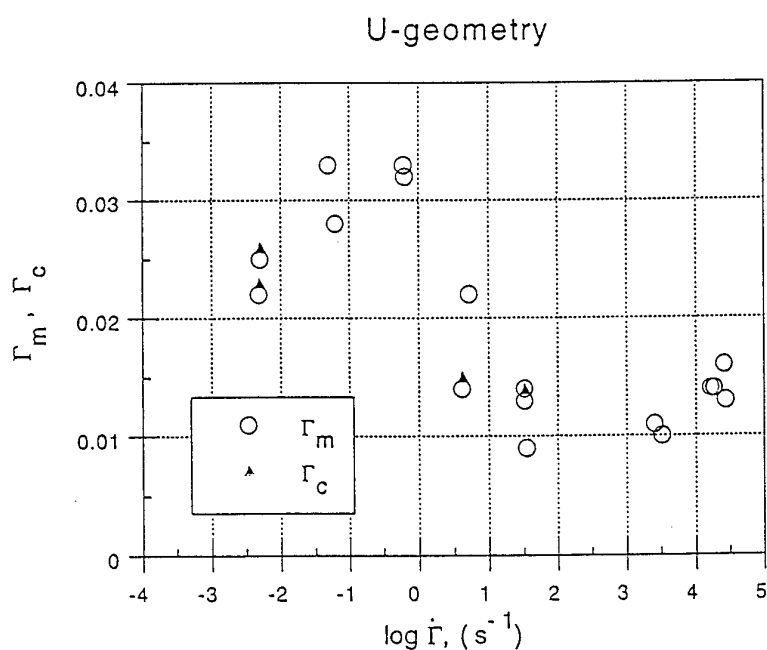
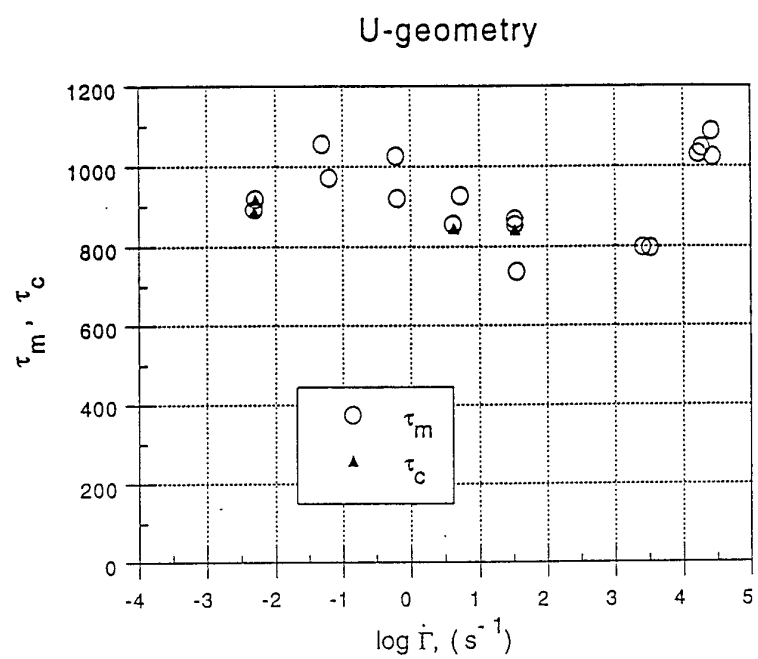


Fig. 11

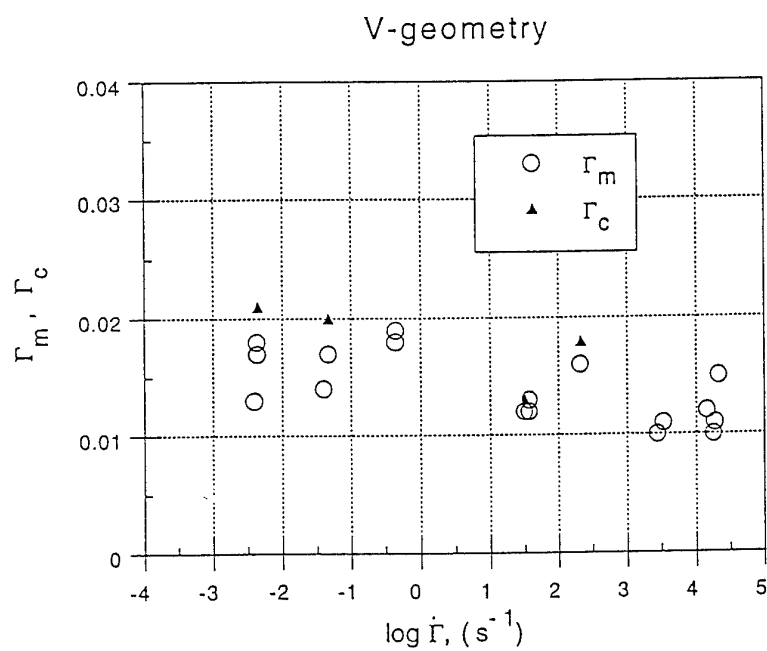
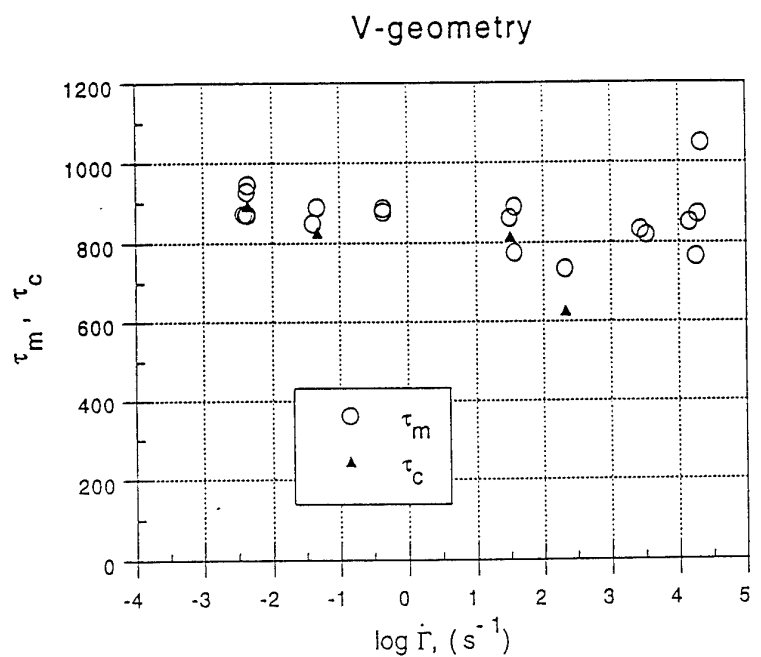


Fig. 12

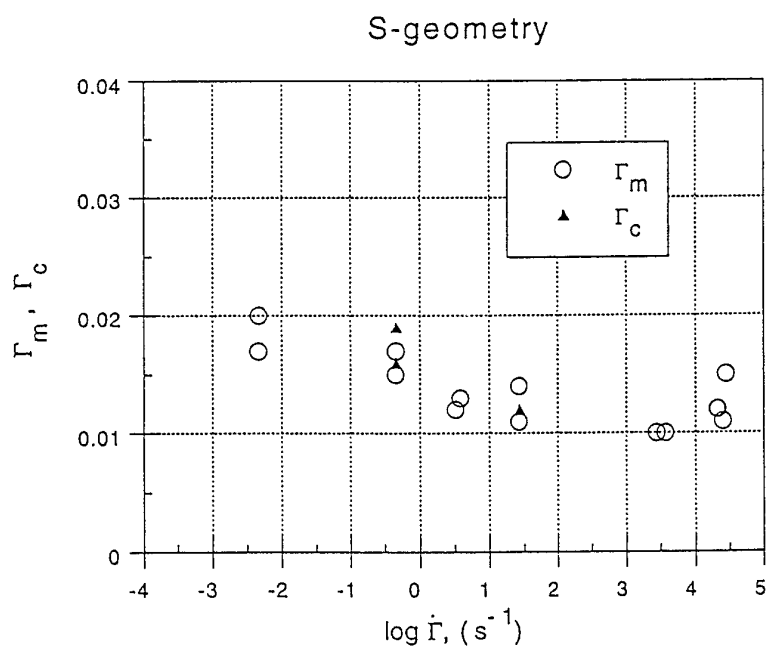
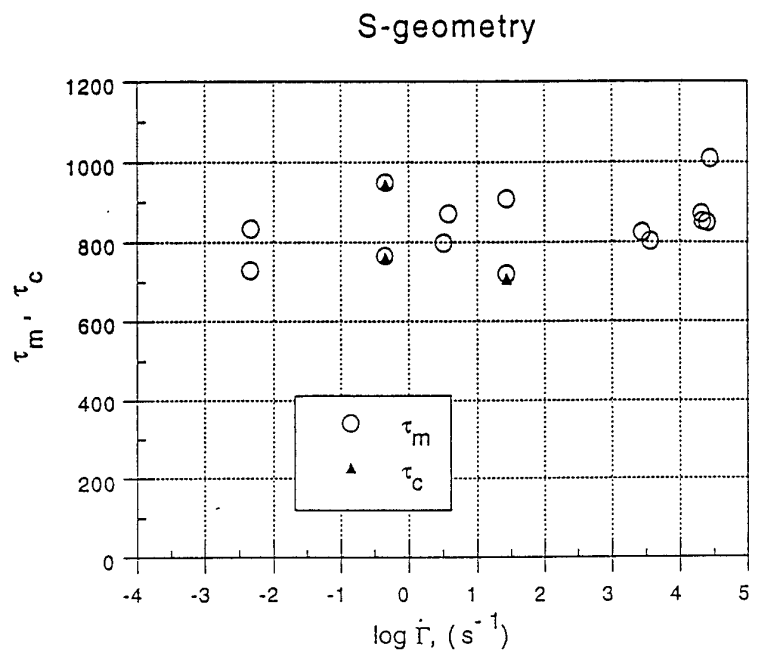


Fig. 13

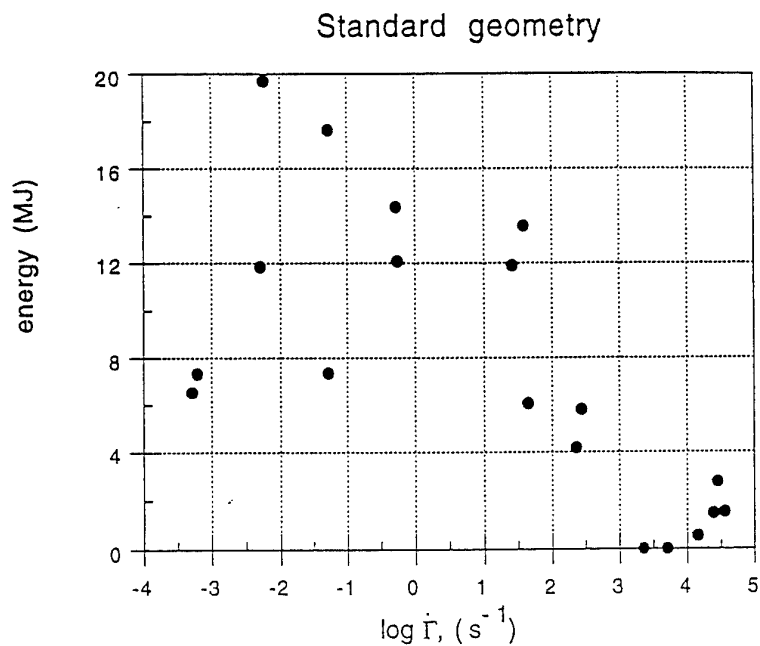


Fig. 14

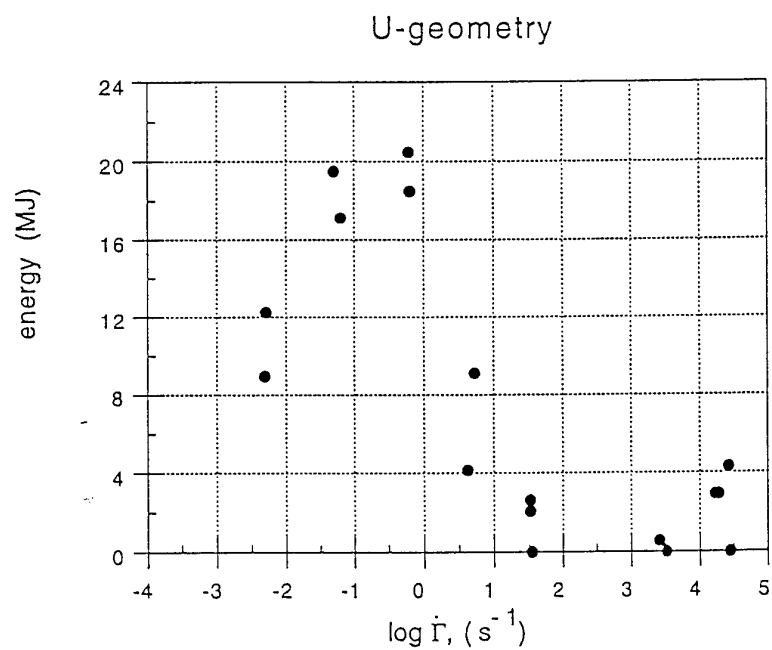


Fig. 15

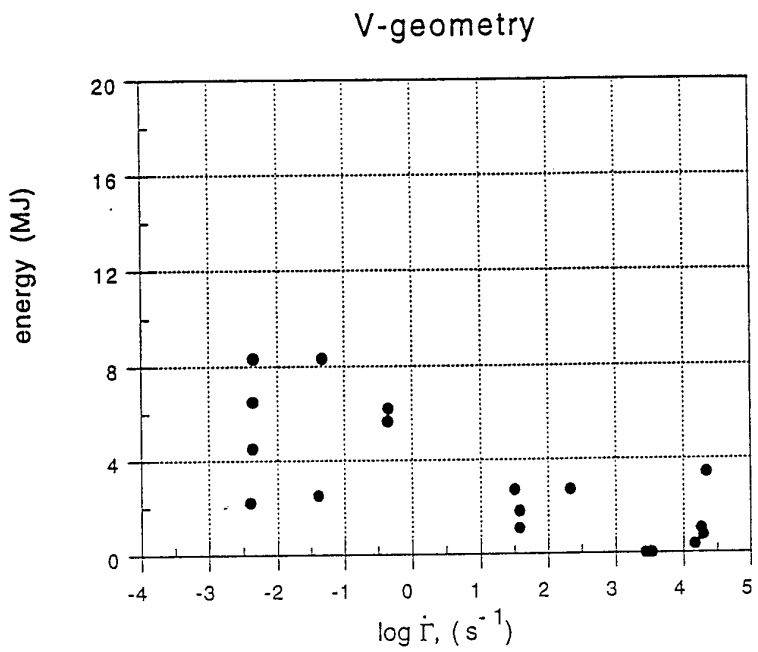


Fig. 16

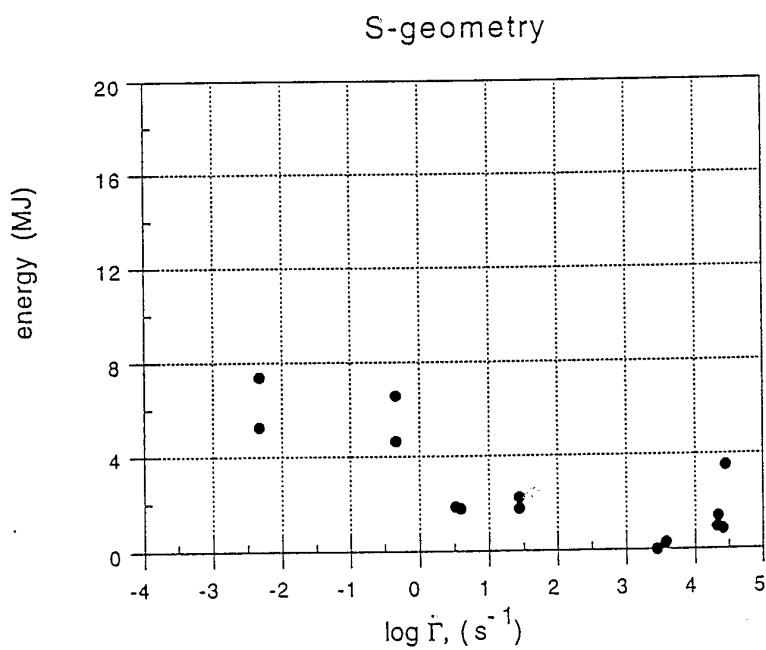


Fig. 17

ABAQUS

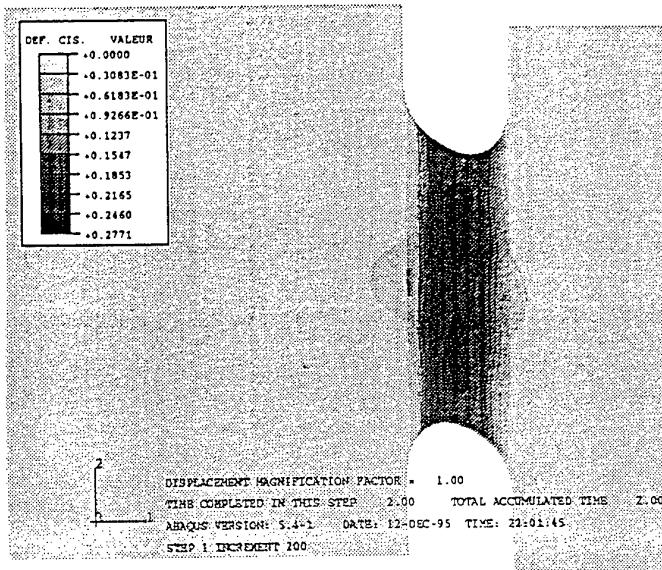
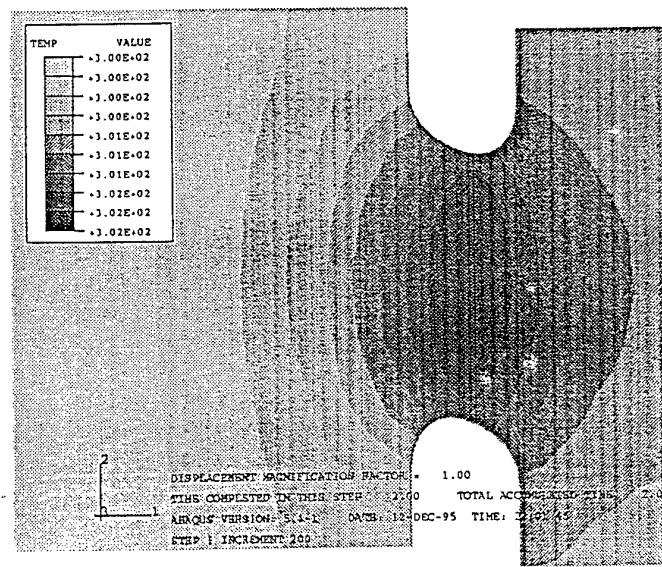


Fig. 18

ABAQUS



ABAQUS

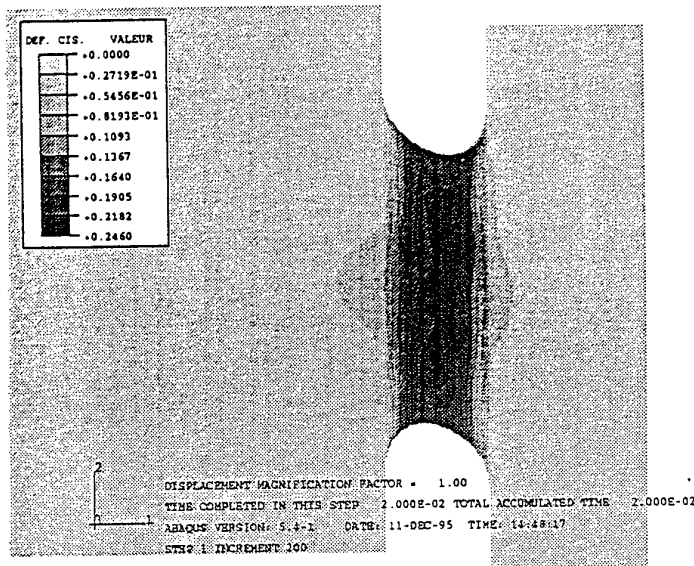
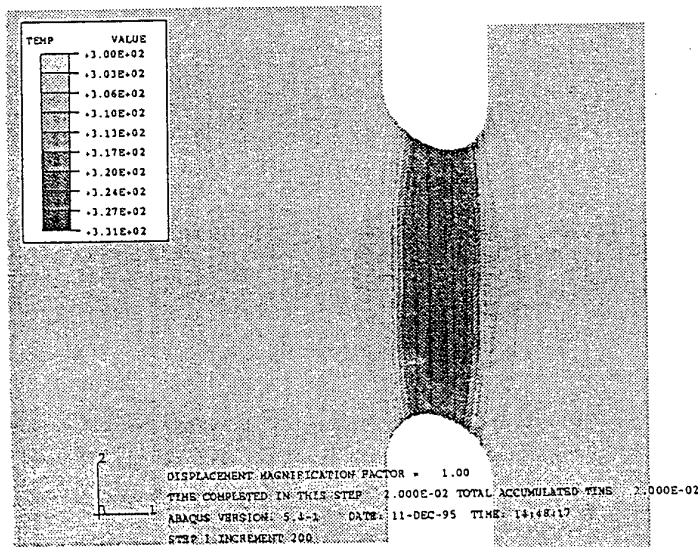


Fig. 19

ABAQUS



ABAQUS

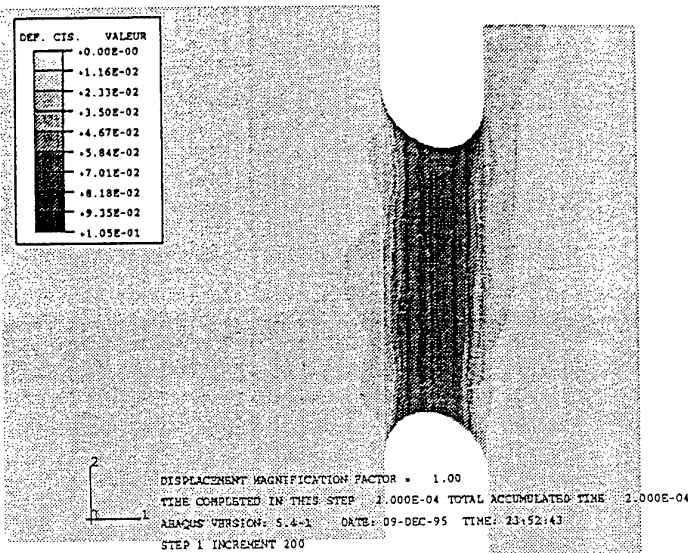
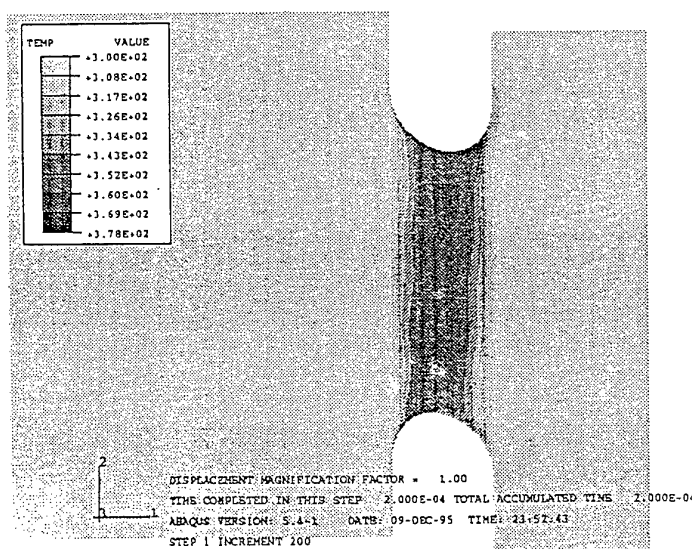


Fig. 20

ABAQUS



ABAQUS

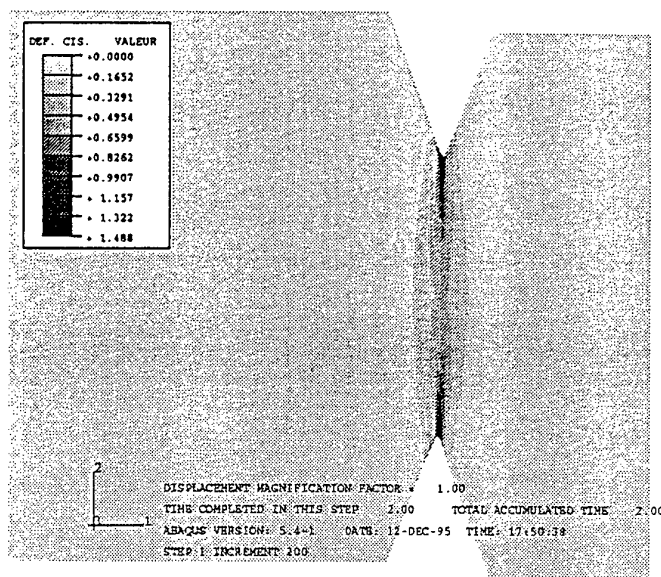
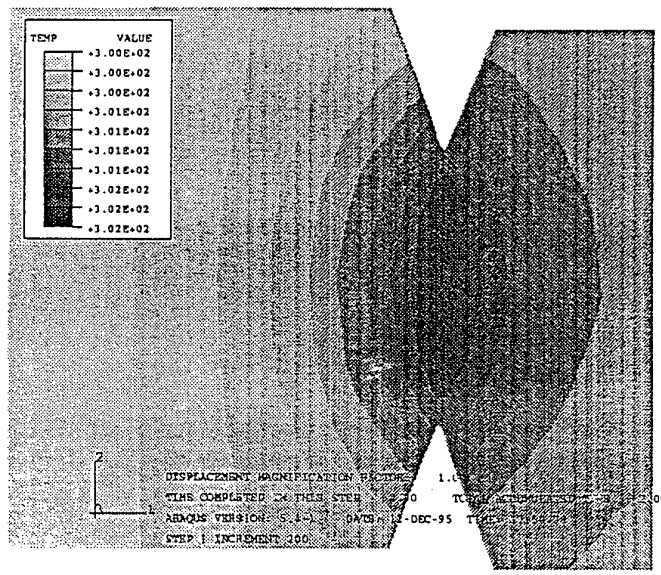


Fig. 21

ABAQUS



ABAQUS

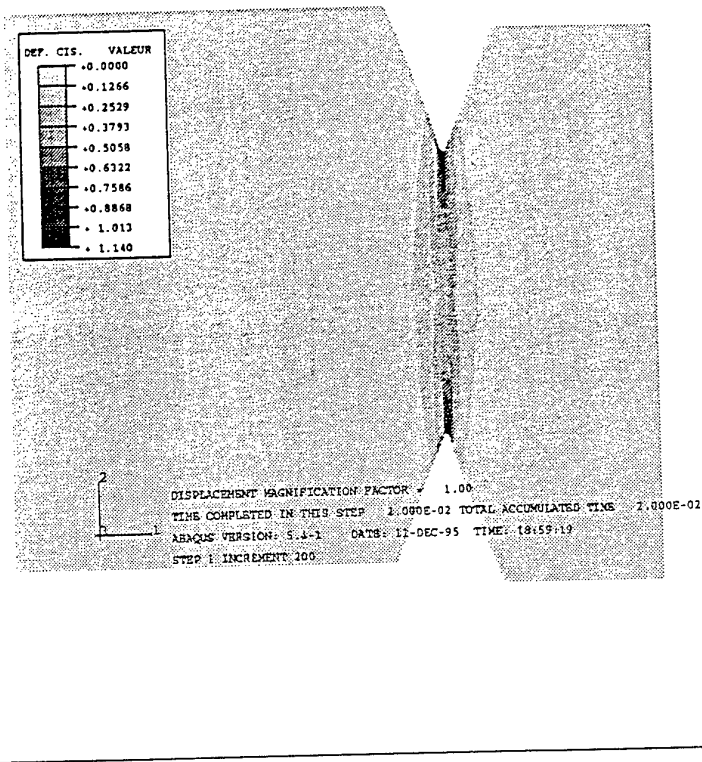
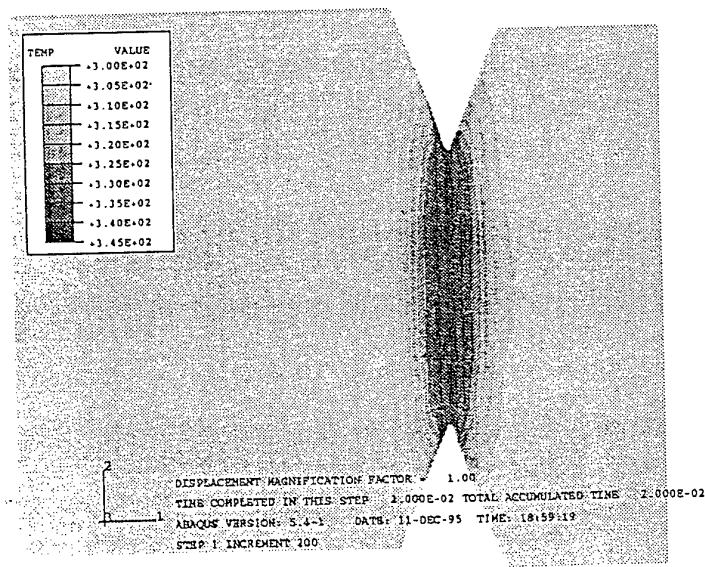


Fig. 22

ABAQUS



ABAQUS

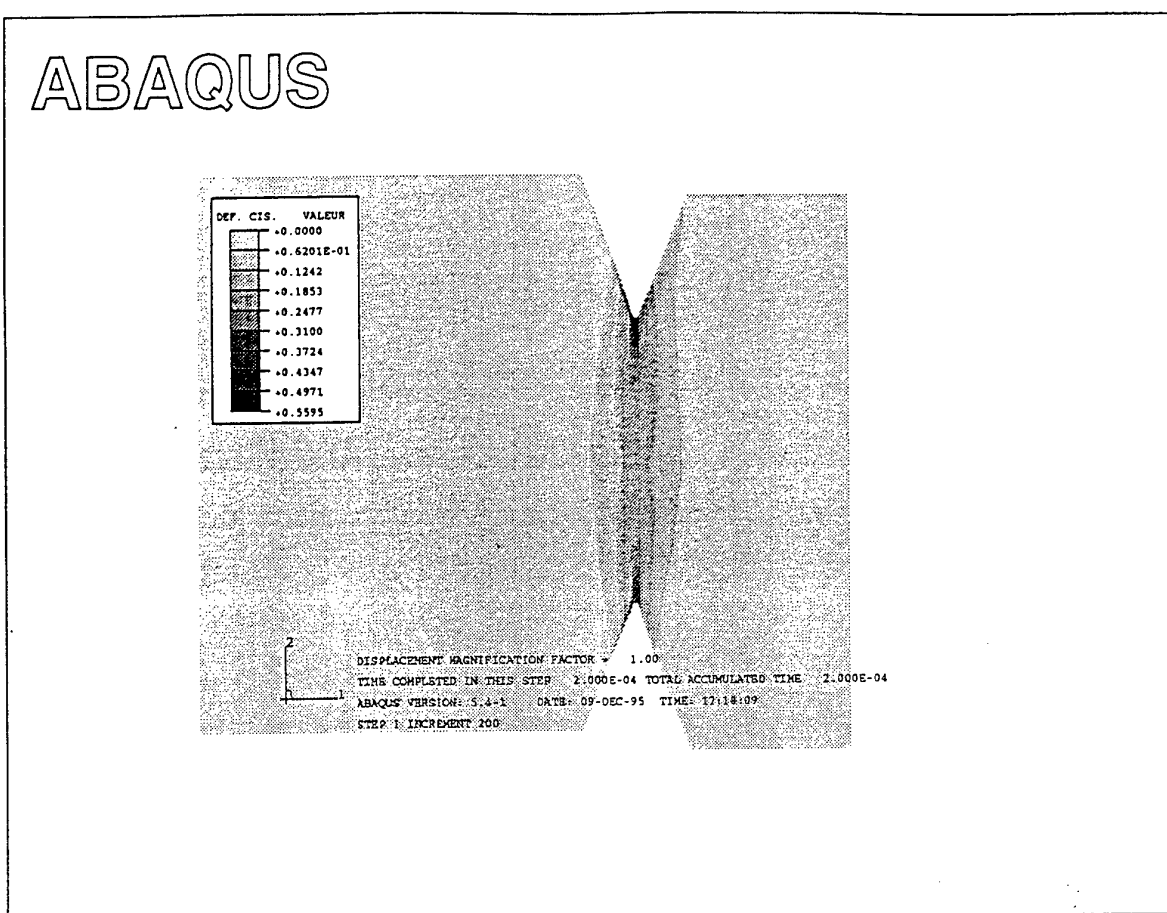
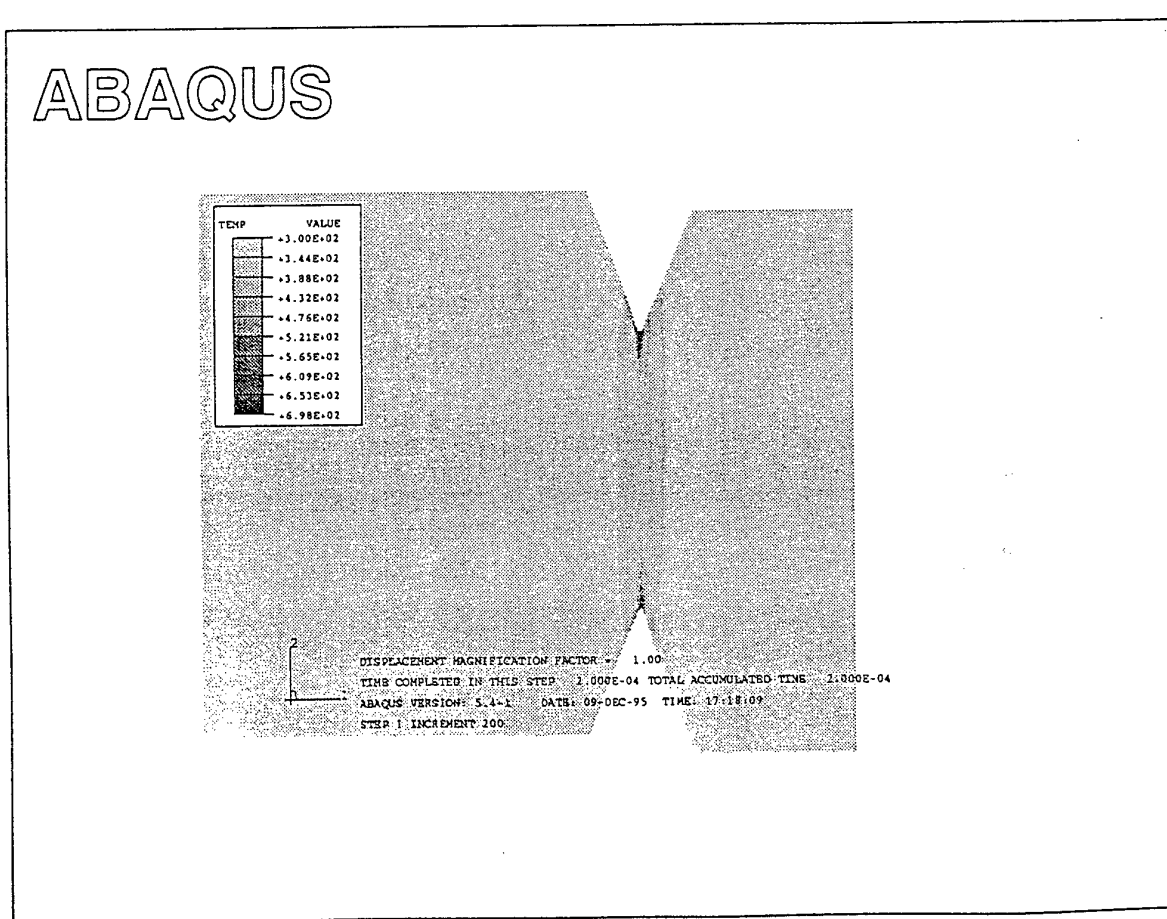


Fig. 23

ABAQUS



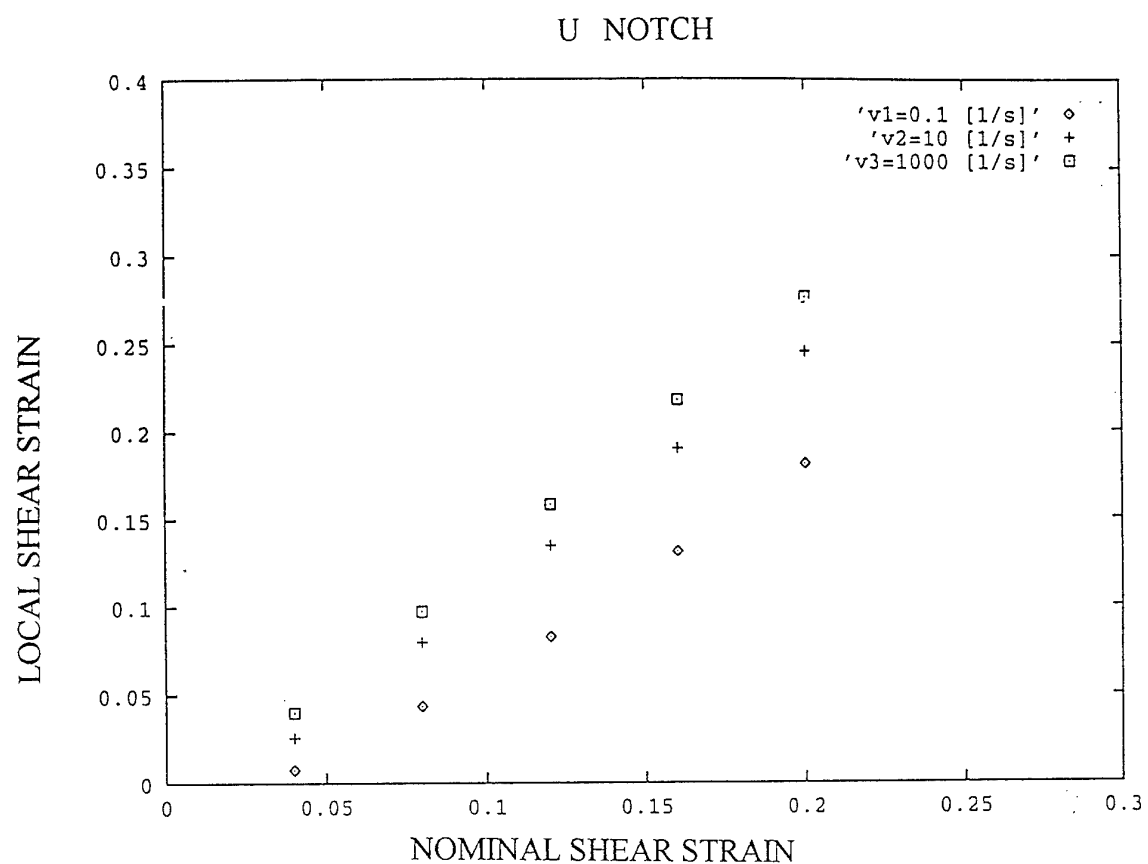
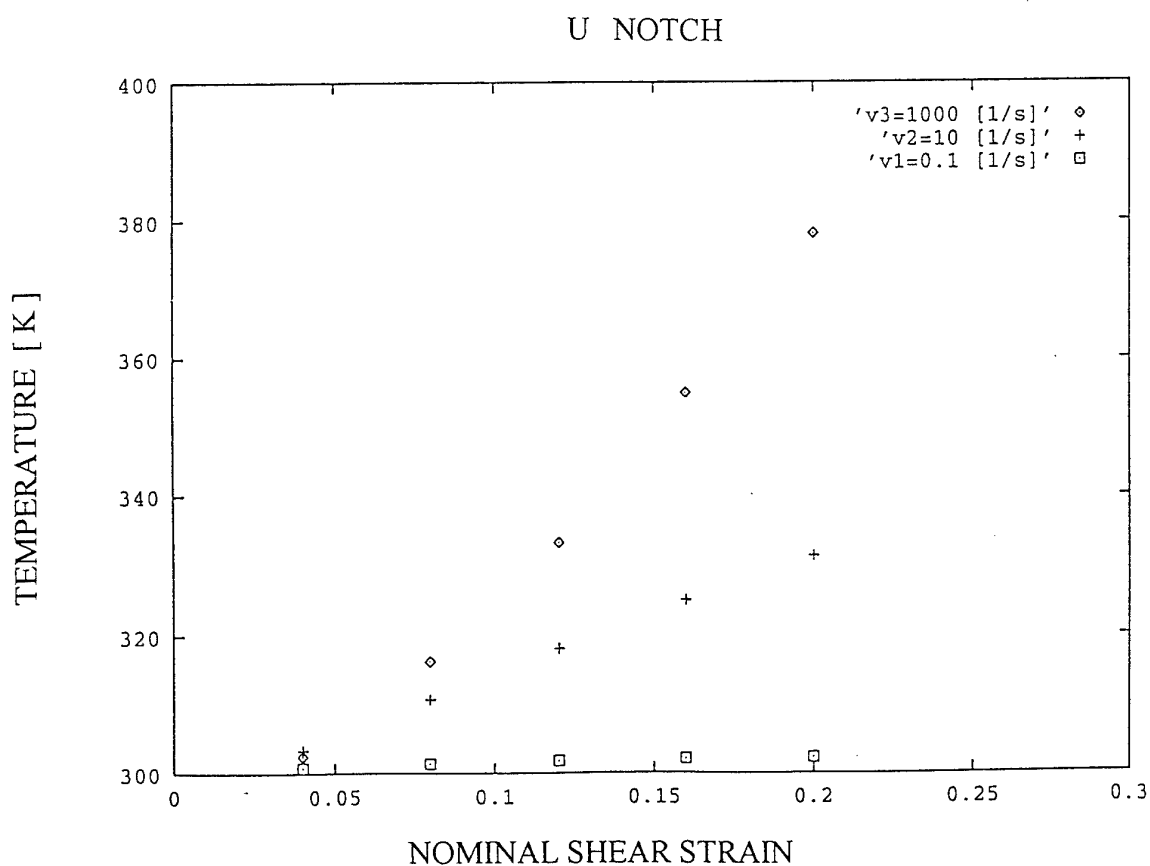


Fig. 24



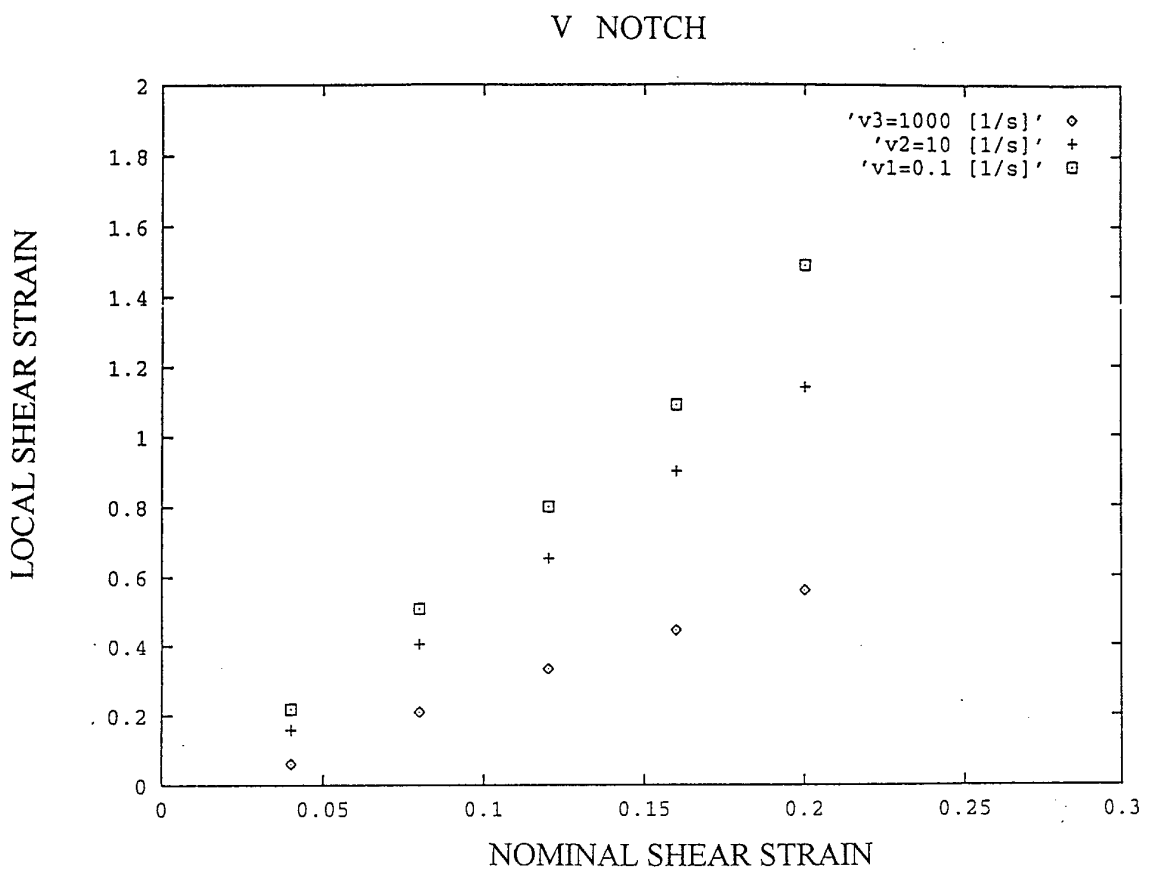
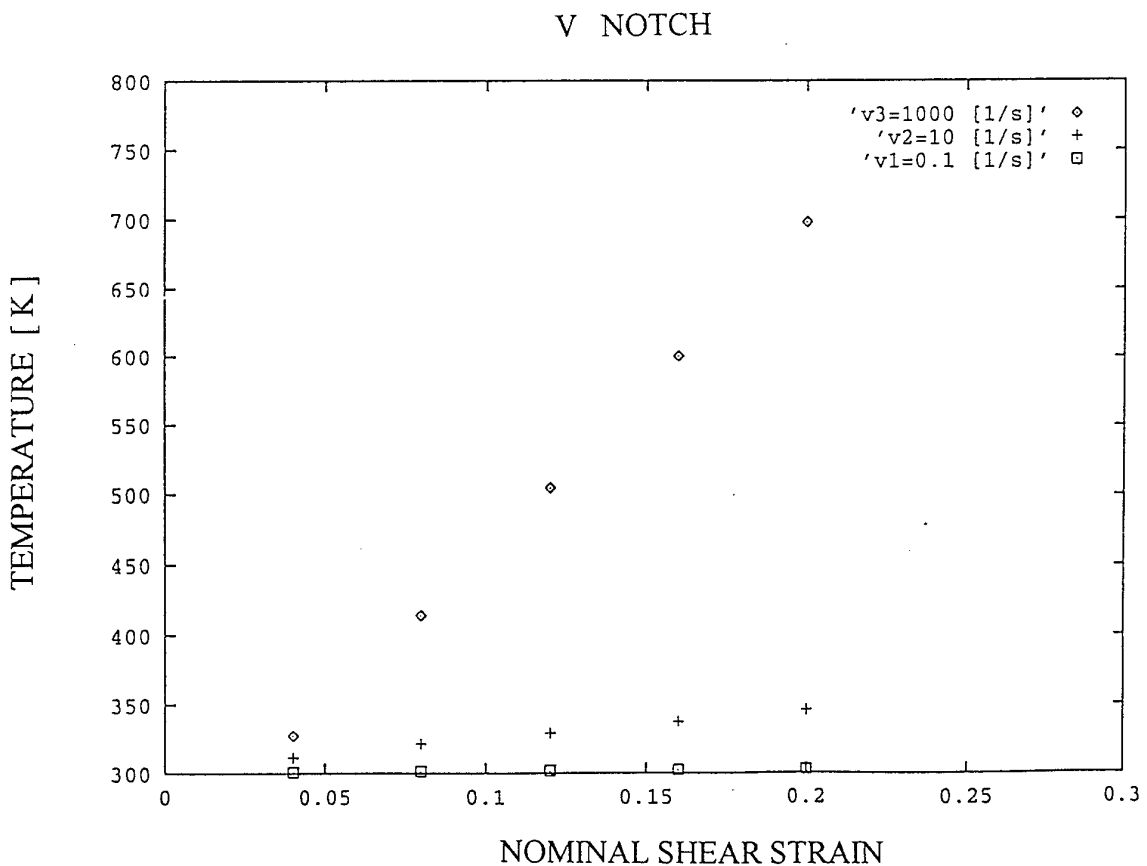


Fig. 25



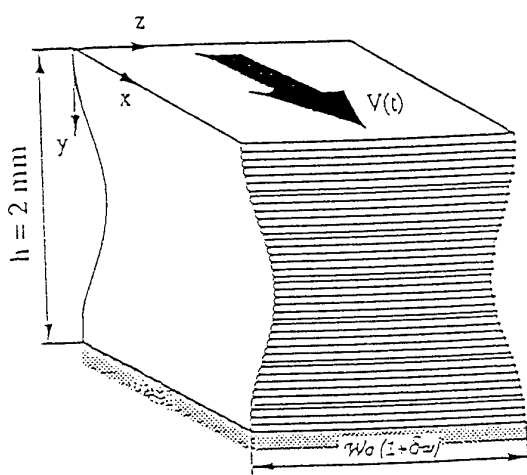


Fig. 26

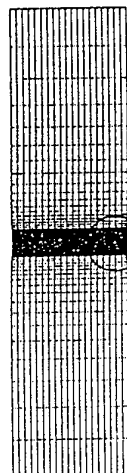
ABAQUS

$y = 0.0$ Boundary Conditions: $V = V_{\text{Impact}}$



$y = 0.02$ Boundary Conditions: $\Delta x = 0$

TYPE OF ELEMENT: CPE4R (or CPE4T)



PROBLEM SIZE

NUMBER OF ELEMENTS IS	1140
NUMBER OF NODES IS	2311
NUMBER OF NODES DEFINED BY THE USER	1230
NUMBER OF INTERNAL NODES GENERATED BY THE PROGRAM	11121
TOTAL NUMBER OF VARIABLES IN THE MODEL	2440
(DEGREES OF FREEDOM PLUS ANY LAGRANGE MULTIPLIER VARIABLES)	
MAXIMUM D.O.F. WAVEFRONT ESTIMATED AS	16
RMS WAVEFRONT ESTIMATED AS	15

Fig. 27

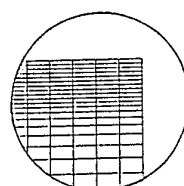
ABAQUS

$y = 0.0$ Boundary Conditions: $V = V_{\text{Impact}}$



$y = 0.02$ Boundary Conditions: $\Delta x = 0$

TYPE OF ELEMENT: CPE4R (or CPE4T)



PROBLEM SIZE

NUMBER OF ELEMENTS IS	665
NUMBER OF NODES IS	1366
NUMBER OF NODES DEFINED BY THE USER	720
NUMBER OF INTERNAL NODES GENERATED BY THE PROGRAM	646
TOTAL NUMBER OF VARIABLES IN THE MODEL	1440
(DEGREES OF FREEDOM PLUS ANY LAGRANGE MULTIPLIER VARIABLES)	
MAXIMUM D.O.F. WAVEFRONT ESTIMATED AS	16
RMS WAVEFRONT ESTIMATED AS	15

Fig. 28

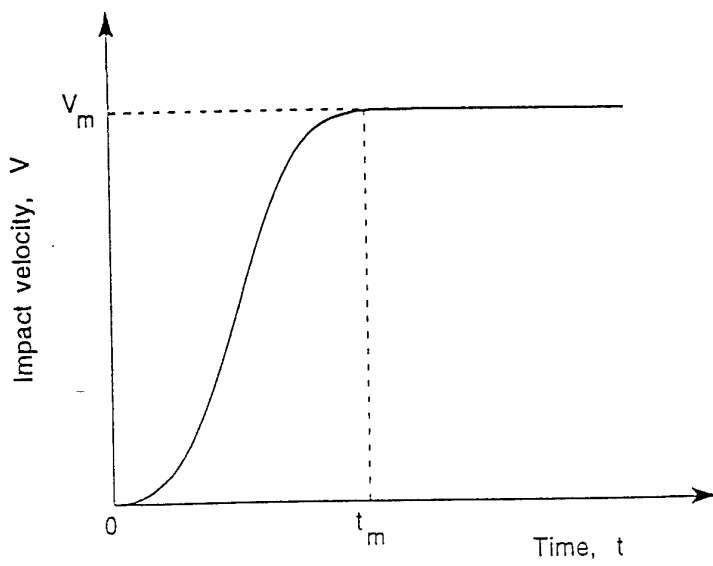


Fig. 29

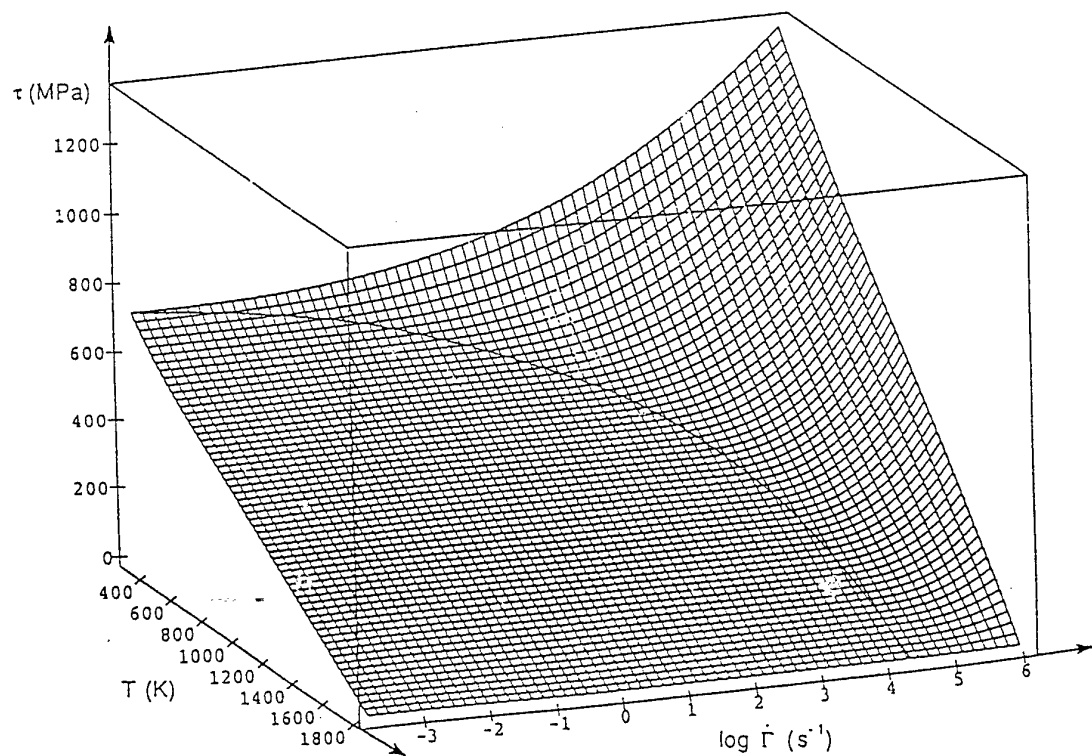


Fig. 30

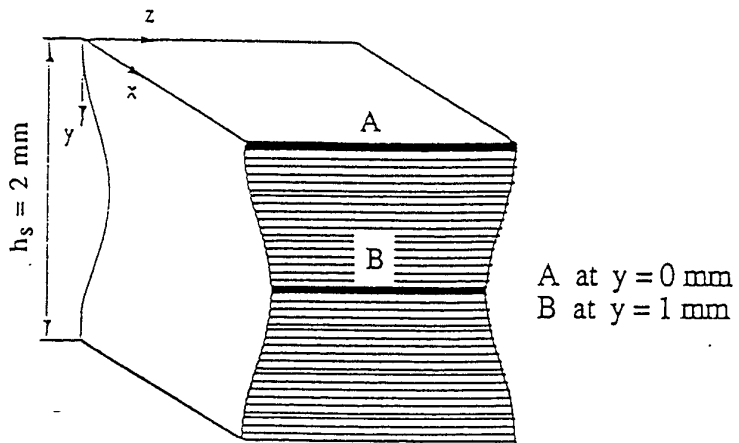


Fig. 31

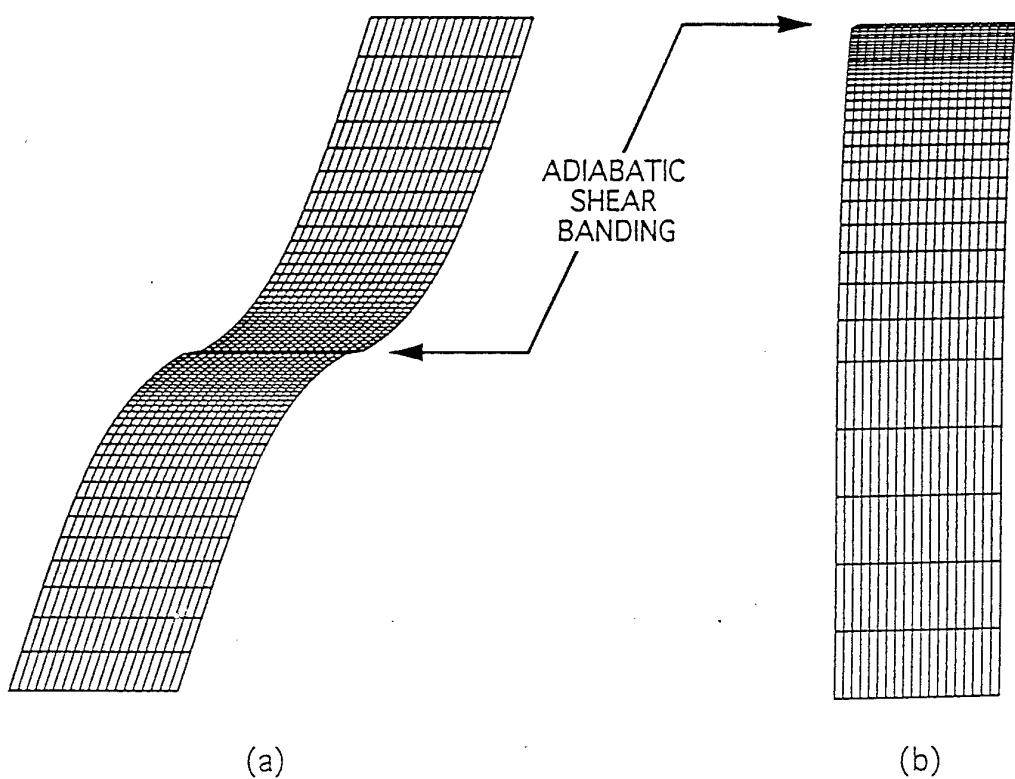


Fig 32

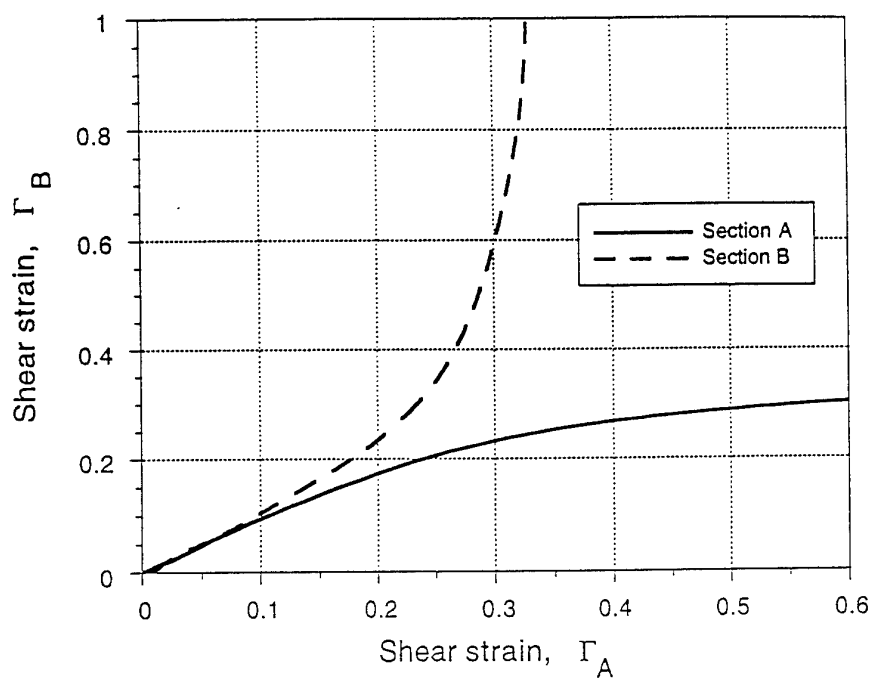


Fig. 33

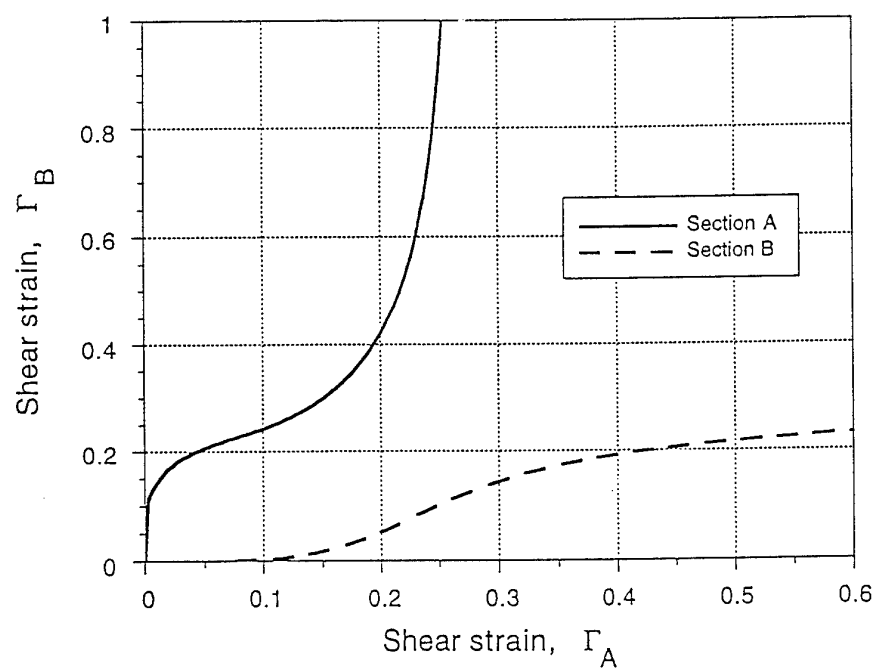


Fig. 34

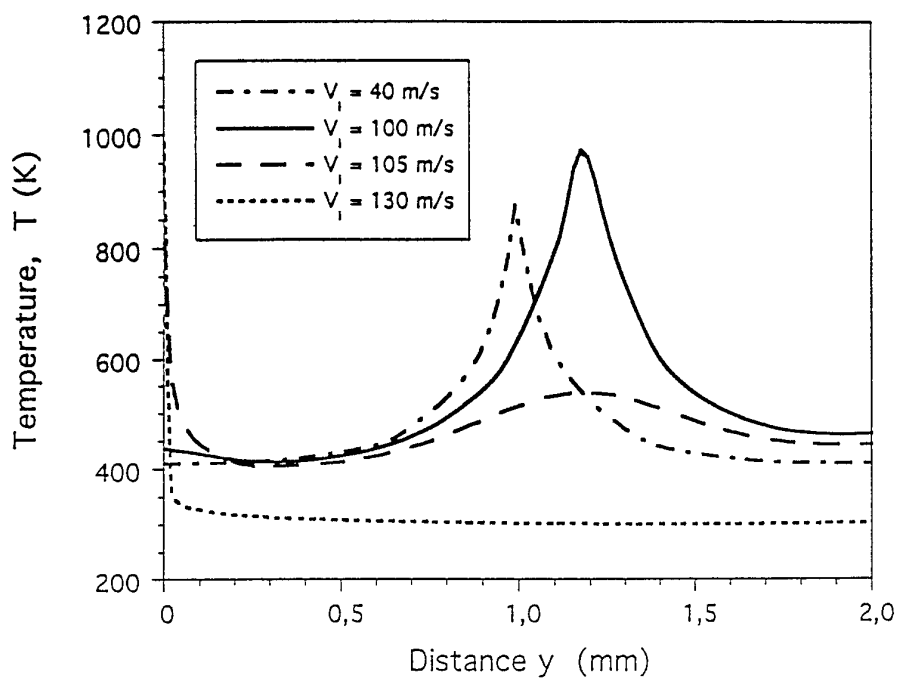


Fig. 36

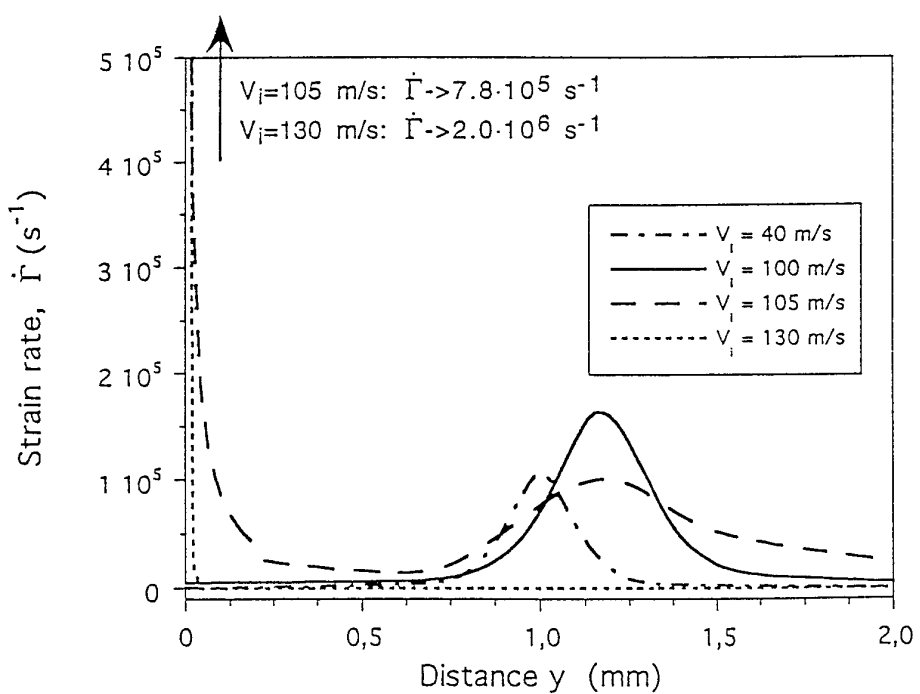


Fig. 35

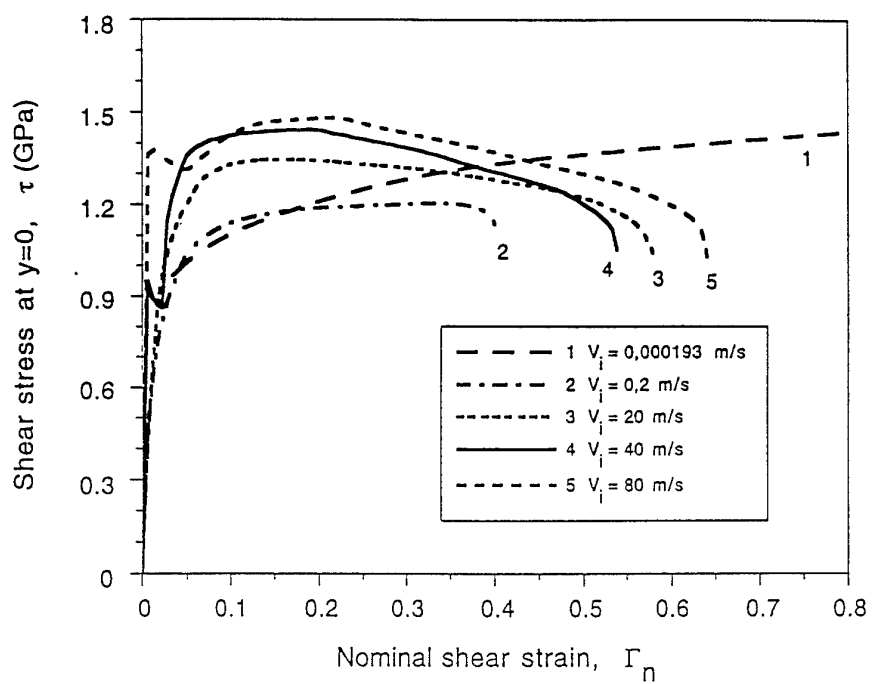


Fig. 37

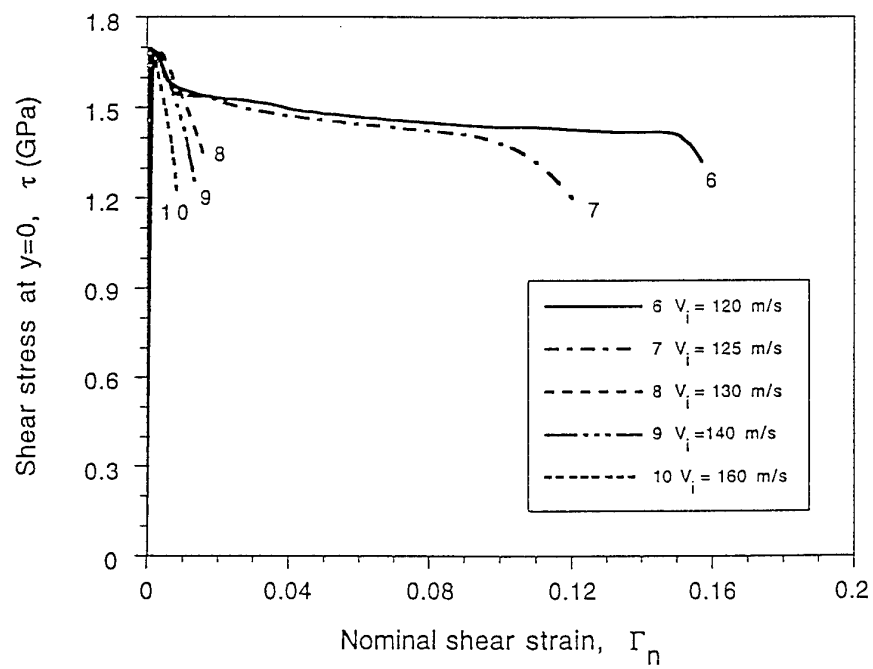


Fig. 38

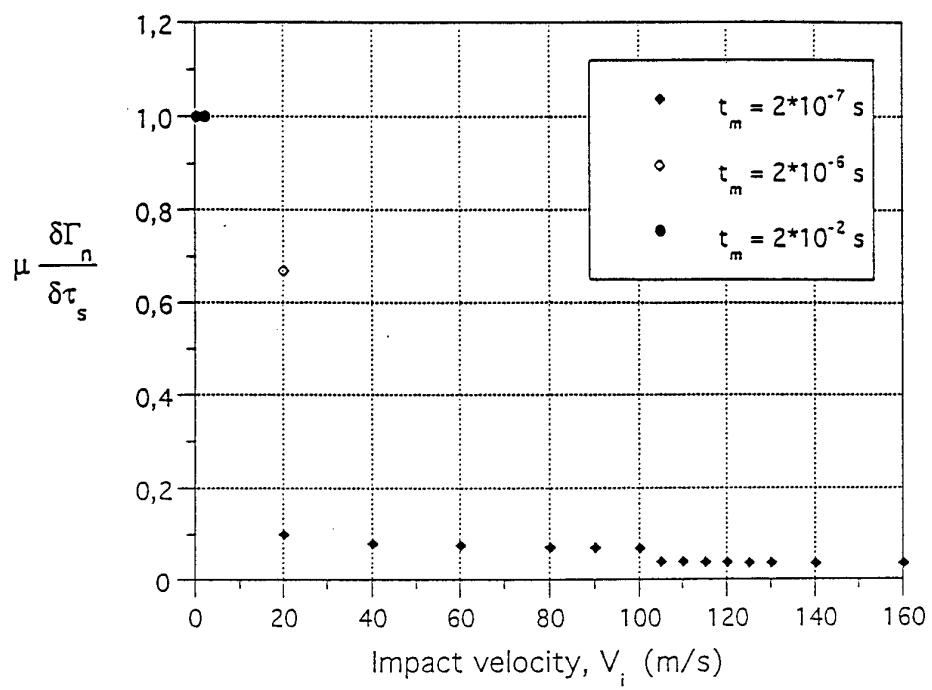


Fig. 39

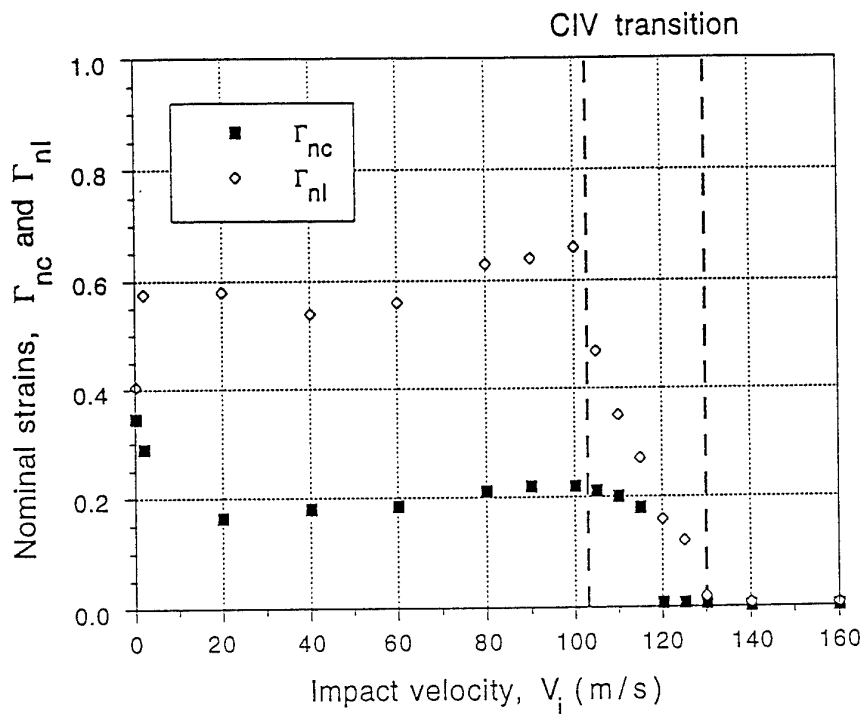


Fig. 40

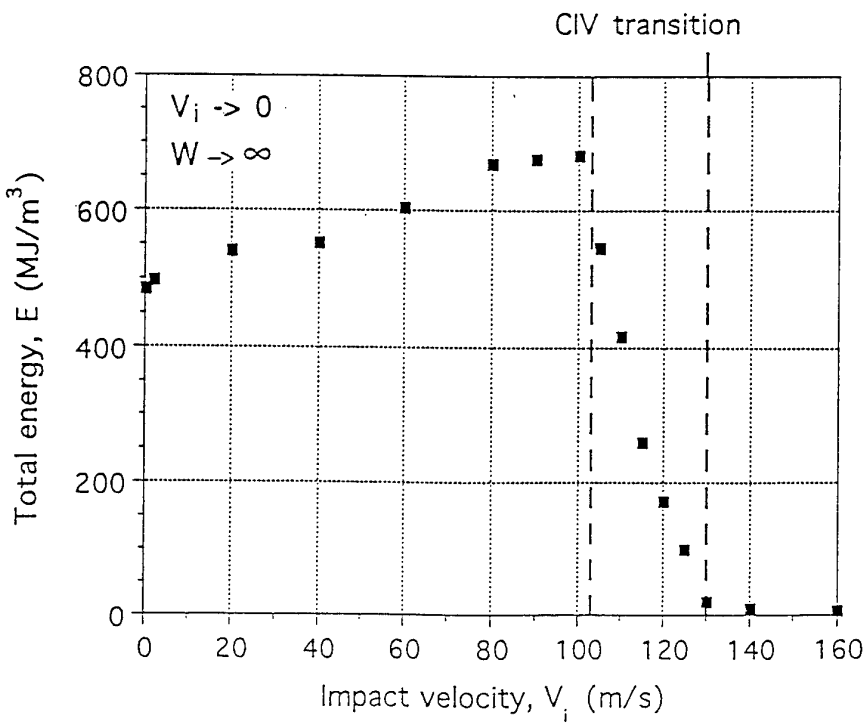


Fig. 41